Article
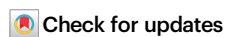
RH3 enhances antiviral defense by facilitating small RNA loading into Argonaute 2 at endoplasmic reticulum–chloroplast membrane contact sites

Juan Huang[1,2,9], Juan Du[1,2,9], Yan Liu[1,3], Lu Lu[1], Yanzhuo Xu[1,2], Jianfei Shi[1,2], Qing Liu[1,2], Qi Li[1], Yang Liu[1,2], Yaqiu Chen[1], Meng Du[1], Yiming Zhao[1,2], Liangxiao Huo[4], Weiran Wang[4], Chenxi Ding[4], Liya Wei[4], Jianguo Wu[5], Yao-Wu Yuan[6], Jinfeng Chen [1], Ruixi Li [7], Feng Cui [1,2] ✉ & Xiaoming Zhang [1,2,8] ✉

While RNA silencing is crucial for plant resistance against viruses, the cellular connections between RNA silencing and antiviral responses in plants remain poorly understood. In this study, we aim to investigate this relationship by examining the subcellular localization of small RNA loading and viral replication in *Arabidopsis*. Our findings reveal that Argonaute 2 (AGO2), a key component of RNA silencing, loads small RNAs at the endoplasmic reticulum (ER)–chloroplast membrane contact sites (MCSs). We identify a chloroplast-localized protein, RNA helicase 3 (RH3), which interacts with AGO2 and facilitates the loading of small RNAs into AGO2 at these MCSs. Furthermore, we discover that MCSs serve as replication sites for certain plant viruses. RH3 also promotes the loading of viral-derived small RNAs into AGO2, thereby enhancing plant antiviral resistance. Overall, our study sheds light on the roles of RH3 in RNA silencing and plant antiviral defenses, providing valuable insights into the cytobiological connections between RNA silencing, viral replication, and antiviral immunity.

RNA silencing is a conserved gene regulation mechanism found across eukaryotes, mediating by small RNAs (sRNAs) associated with Argonaute (AGO) proteins, which are effectors of the RNA-induced silencing complex (RISC). These sRNAs, typically 20-30 nucleotides long, are processed from double-stranded RNAs (dsRNAs) by Dicer or Dicer-like (DCL) proteins[1,2]. In plants, sRNAs originated from endogenous sources can be classified into different subgroups, including micro-RNAs (miRNAs), phased siRNAs (phasiRNAs), and heterochromatin

[1]State Key Laboratory of Integrated Management of Pest Insects and Rodents, Institute of Zoology, Chinese Academy of Sciences, Beijing 100101, China. [2]College of Life Science, University of Chinese Academy of Sciences, Beijing 100049, China. [3]Institute of Plant Protection, Shandong Academy of Agricultural Sciences, Jinan 250100, China. [4]College of Life Sciences, Hebei University, Baoding, Hebei 071002, China. [5]Vector-borne Virus Research Center, Fujian Province Key Laboratory of Plant Virology, Fujian Agriculture and Forestry University, Fuzhou 350002, China. [6]Department of Ecology and Evolutionary Biology, University of Connecticut, 75 North Eagleville Road, Unit 3043, Storrs, CT 06269, USA. [7]SUSTech-PKU Institute of Plant and Food Science, Department of Biology, Southern University of Science and Technology, Shenzhen, Guangdong 518055, China. [8]Hainan Seed Industry Laboratory, Sanya 572025, China. [9]These authors contributed equally: Juan Huang, Juan Du. ✉e-mail: cuif@ioz.ac.cn; zhangxm@ioz.ac.cn

siRNAs (hc-siRNAs)[3–5]. Additionally, sRNAs can be generated from exogenous sources, such as viruses, and function in defense against these pathogens. During the replication of RNA viruses or transcription of DNA viruses, abundant dsRNAs are generated and processed into virus-derived small interfering RNAs (vsiRNAs)[3,6,7]. Despite the well-established importance of RNA silencing in plant antiviral responses, the cytobiological connections between RNA silencing and plant antiviral immunities remain poorly understood.

The loading of sRNAs into specific AGO proteins is a crucial step in RNA silencing-mediated gene regulation[3,4]. Different AGO proteins have been shown to load specific types of sRNAs at distinct subcellular localizations. For example, *Arabidopsis* AGO1 loads miRNAs in the nucleus and trans-acting siRNAs (ta-siRNA, a type of phasiRNAs) in the cytoplasm[8], while AGO4 loads hc-siRNAs in the cytoplasm[9,10]. AGO2 loads various types of sRNAs and is involved in host resistance to bacteria and DNA repair processes[11,12]. AGO2 also associates with vsiRNAs and plays pivotal roles in the antiviral immune response[13–19]. However, the subcellular localizations for sRNA loading into AGO2 remain undetermined.

Eukaryotic cells are characterized by the presence of membrane-bound organelles, which compartmentalize the cell and carry out specialized functions[20–22]. The endoplasmic reticulum (ER) is the largest organelle and is involved in protein synthesis and folding, lipid and steroid synthesis, and calcium storage and release[23,24]. *Arabidopsis thaliana* AGO1, an essential component of RNA silencing, has been shown to localize to the ER, where it inhibits the translations and cleavage miRNA target transcripts[25–27]. Chloroplasts, which evolved from endosymbiotic cyanobacteria[28], lack typical RNA silencing machinery[29] but can provide necessary molecules[28,30] or spatial compartments for RNA silencing. Membrane contact sites (MCSs) between organelles, where different organelles are physically tethered but do not fuse, allow for communication and coordination between organelles[21,22,31]. The ER and chloroplasts can form unique ER-chloroplast MCSs in plants[32–35], although their specific roles in biological processes still need to be investigated[36,37].

In this study, we investigated the subcellular localizations where sRNAs are loaded into AGO2 and their relationship with viral replication sites. Through immunoprecipitation (IP) coupled with mass spectrometry (MS) assays, we identified RH3, a DEAD-box RNA helicase localized in the chloroplast, interacting with AGO2 at ER–chloroplast MCSs. Further experiments involving microsomal membrane fractionation and sRNA pulldown assays revealed that AGO2 loads sRNAs at the ER–chloroplast MCSs, and RH3 facilitates their loading at the same sites. Additionally, protein co-localization and fluorescence in situ hybridization (FISH) assays demonstrated that the replication of certain viruses occurs at the ER–chloroplast MCSs. RH3 facilitates the loading of vsiRNAs into AGO2, thereby contributing to antiviral immunity. Together, this study provides valuable insights into the cytobiological aspects of RNA silencing in the context of host defense against viruses.

Results
Chloroplast-localized RH3 interacts with AGO2
To explore the sRNA loading mechanism and the involvement of chloroplast in RNA silencing, we employed a combination of AGO2 IP with MS to identify proteins associated with AGO2 (Supplementary Fig. 1). We performed IP-MS assay on *pAGO2::HA-AGO2 in ago2-1* and *p35S::3HA-GFP in* Col-0, and identified 44 candidate proteins (fold change > 2, p < 0.05) (Supplementary Fig. 2 and Supplementary Data 1). Among these candidate proteins, we focused on RH3, a conserved chloroplast-localized DEAD-box RNA helicase protein in plants (Supplementary Figs. 2, 3). RNA helicases are known to participate in various RNA-related processes by modulating RNA or RNA-protein complex structures[38,39]. Given the potential involvement of RNA helicases in sRNA loading, we selected RH3 for further analysis.

To investigate the interaction between RH3 and AGO2, we conducted co-immunoprecipitation (Co-IP) experiments in *Nicotiana benthamiana* plants. We used chloroplast-localized BFA1-FLAG as a control for RH3[40]. The Co-IP assay successfully demonstrated the pull-down of RH3 by AGO2 (Fig. 1a, middle panel), indicating their interaction. Similarly, the reciprocal Co-IP experiment showed the pull-down of AGO2 by RH3 (Fig. 1a, right panel). Furthermore, Co-IP assays were performed in transgenic *Arabidopsis* plants expressing *pAGO2::HA-AGO2* in the *ago2-1* mutant background, with *p35S::3HA-GFP* in Col-0 plants as a control. The results showed that RH3 protein was only detected in HA-AGO2 IP fractions (Fig. 1b), providing additional evidence for the association between RH3 and AGO2.

To investigate the direct interaction between RH3 and AGO2, we conducted in vitro pulldown assays using recombinant proteins purified from *Escherichia coli* cell cultures (Supplementary Figs. 4, 5a). When FLAG-AGO2 was incubated with RH3-HA or glutathione S-transferase (GST)-HA, a strong RH3-HA signal was detected on the FLAG-AGO2 beads, while no GST-HA signal was observed (Fig. 1c). Moreover, deletion of residues 451-500 in RH3 resulted in a decreased interaction (Supplementary Fig. 5b–f). Additionally, the association of RH3 with AGO2 was reduced when the K459A, R460A, R463A, and R467A mutations were introduced simultaneously (Fig. 1d, e, and Supplementary Fig. 5g). Coexpressing HA-AGO2 with mRH3-FLAG (K459A, R460A, R463A and R467A) or with wild-type RH3-FLAG in *N. benthamiana* plants demonstrated that the accumulation of mRH3 in the HA-AGO2 groups decreased by 45.1% compared to that of wild-type RH3 (Fig. 1f, g), indicating the importance of these residues in the association between RH3 and AGO2. These findings provide evidence that AGO2 directly interacts with RH3.
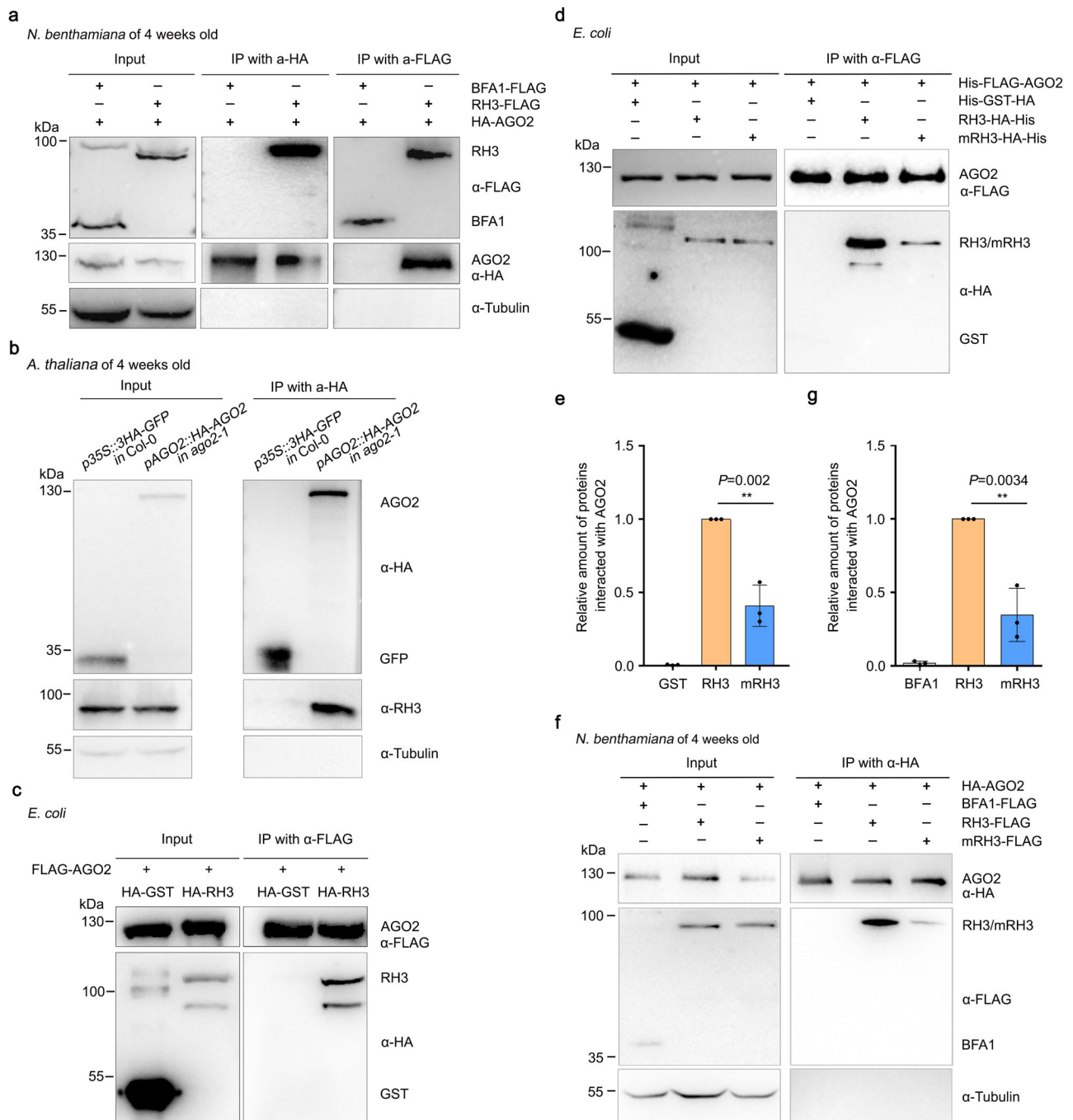
RH3 interacts with AGO2 at chloroplast periphery
To investigate the subcellular localization where the RH3-AGO2 interaction occurs, we examined the localization patterns of RH3 and AGO2. While RH3 is predominantly localized in the chloroplast, a fraction of RH3 was observed to localize at the chloroplast periphery when transiently expressed in the *Arabidopsis* protoplasts (Supplementary Fig. 6a). This localization pattern was confirmed through immunofluorescence assays using an anti-FLAG antibody in *pRH3::RH3-FLAG in rh3-4* plants (Fig. 2a). Co-labeling RH3 with Toc34, a marker for the chloroplast outer membrane[41], further demonstrated the localization of RH3 at the chloroplast periphery (Fig. 2b). Immunoelectron microscopy assays also revealed the presence of RH3 particles in the envelope area of the chloroplast (Fig. 2c). Similarly, transient expression assays in *Arabidopsis* protoplasts (Supplementary Fig. 6a) and immunofluorescence assays using an anti-HA antibody in *pAGO2::HA-AGO2 in ago2-1* plants (Fig. 2d) showed that AGO2 disperses around the chloroplast periphery.

To further examine the co-localization of RH3 and AGO2, we performed immunofluorescence assay using anti-FLAG and anti-AGO2 antibodies in *pRH3::RH3-FLAG in rh3-4* plants. The specificity of the anti-AGO2 antibody was confirmed using a dual labeling assay (Supplementary Fig. 6b). The results showed that a portion of RH3 co-localized with AGO2 at the chloroplast periphery (Fig. 2e and Supplementary Fig. 6c, d). Furthermore, a bimolecular fluorescence complementation (BiFC) assay revealed an interaction between RH3 and AGO2 at the chloroplast periphery (Fig. 2f and Supplementary Fig. 7).

RH3 interacts with AGO2 at ER–chloroplast MCSs
We observed that the BiFC signal of the RH3-AGO2 interaction at the chloroplast periphery displayed an uneven distribution (Fig. 2f). By expressing the commonly used ER marker RFP-HDEL[42], we found that the ER contacts the chloroplasts at discontinuous subdomains (Supplementary Fig. 8a). Considering the physical connection between the ER and the chloroplasts and the localization of *Arabidopsis* AGO1 to the ER[26], we hypothesized that the uneven localization of the RH3-AGO2

Fig. 1 | Chloroplast-localized RH3 interacts with AGO2. a Co-IP assays in *N. benthamiana* plants showed the RH3-AGO2 interaction. IP was conducted using anti-HA agarose beads to pull down RH3 (middle panel) or anti-FLAG agarose beads to pull down AGO2 (right panel). BFA1 was used as the negative control. **b** In vivo Co-IP assay revealed the interaction of RH3 with AGO2. IP was conducted with anti-HA agarose beads. **c** Pull-down assays using recombinant proteins purified from *E. coli* revealed the direct interaction of RH3 with AGO2. FLAG-tagged AGO2 was pulled down using anti-FLAG agarose beads. RH3 and control GST proteins were probed with anti-HA antibody. **d–g** The simultaneous mutation of K459A, R460A, R463A, and R467A (mRH3) significantly decreased the interaction between RH3 with AGO2. Pull-down assays were performed using recombinant proteins purified from *E. coli* (**d, e**) and proteins transiently expressed in *N. benthamiana* (**f, g**). The quantitative data for (**d**) and (**f**) and another two replicates were used to form (**e**) and (**g**) respectively (n = 3). Errors bars are mean ± SD. Student's *t* test was performed to determine statistical significance. **, $P < 0.01$. Source data are provided as a Source Data file.
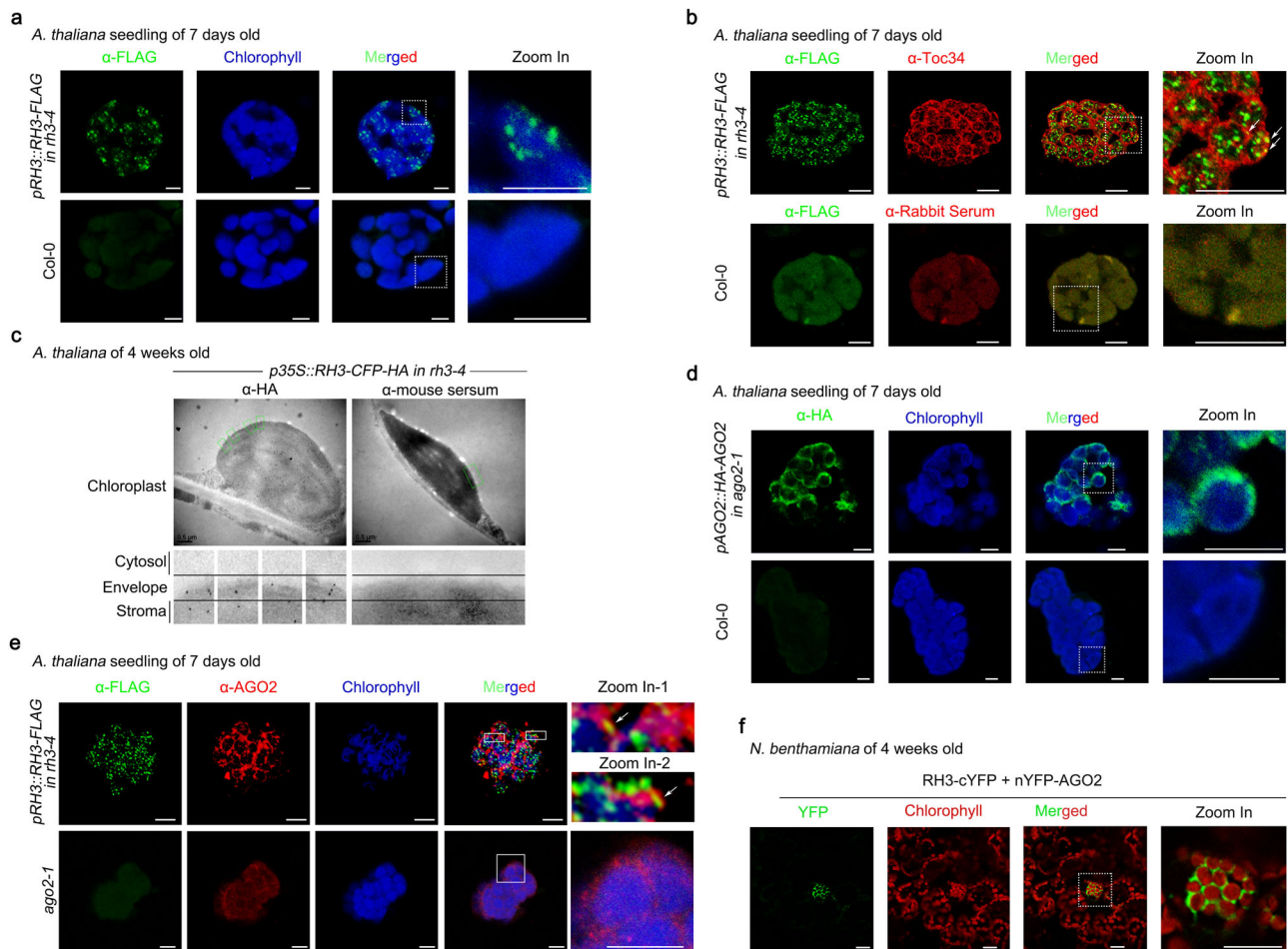
interaction at the chloroplast periphery related to ER-chloroplast contact sites.

To test this hypothesis, we first determined the potential subcellular localization of AGO2 with the ER. AGO2-YFP was co-expressed with RFP-HDEL in *N. benthamiana*. As shown in Fig. 3a, YFP-AGO2 signals exhibited a net-like pattern that was identical to RFP-HDEL in both epidermal and mesophyll cells. Immunofluorescence assays in

transgenic plants expressing GFP-HDEL also showed that AGO2 associates with GFP-labeled ER signals, particularly at the chloroplast periphery (Fig. 3b and Supplementary Fig. 8b). These results demonstrate that AGO2 is distributed around the ER network.

Next, we examined whether the interaction between RH3 and AGO2 occurs at the ER juxtaposed to the chloroplast. In epidermal cells lacking chloroplasts, the colocalization of RH3 and AGO2 (Fig. 3c) and

Fig. 2 | RH3 interacts with AGO2 at chloroplast periphery.
a Immunofluorescence analysis of the localization of RH3 in fixed *pRH3:RH3-FLAG in rh3-4*. RH3 was labeled with anti-FLAG antibody (green). **b** Immunofluorescence analysis of the subcellular localization of RH3 and Toc34. RH3 protein particles were labeled with anti-FLAG antibody (green), and Toc34 was labeled with anti-Toc34 antibody (red). Arrows indicate colocalization sites. **c** Immunoelectron microscopy analysis of the subcellular localization of RH3 in the chloroplast of *p35S::RH3-CFP-HA in rh3-4* transgenic *A. thaliana*. RH3 particles were labeled with anti-HA antibody. Four zoom-in sections of the chloroplast periphery labeled by green rectangles were shown at the lower panel, with RH3 particles were observed at the chloroplast periphery. A negative control was performed under the same condition without anti-HA antibody. **d** Immunofluorescence analysis of the localization of AGO2 in fixed *pAGO2:HA-AGO2 in ago2-1*. AGO2 was labeled with anti-HA antibody (green). **e** Immunofluorescence analysis of the colocalization of RH3 and AGO2 in fixed *pRH3:RH3-FLAG in rh3-4*. The upper panel displays a three-dimensional rendering of a 5.6-μm-thick slice, consisting of overlapping 10 layers of 0.4 μm each. RH3 was labeled with anti-FLAG antibody (green), and AGO2 was labeled with anti-AGO2 antibody (red). Two zoom-in sections marked by white rectangles were shown at the right panels. The images of each layer were shown in Supplementary Fig. 6c, d. **f** RH3 and AGO2 interacts at the chloroplast periphery in *N. benthamiana*. Scale bar: **a**, **b**, **d**, **e** and **f**, 5μm; **c**, 0.5 μm. These experiments were repeated three times, yielding similar results.

the BiFC YFP signal of RH3-AGO2 (Fig. 3d) were observed at ER-mesh junctions, suggesting that the ER serves as the anchoring platform for their interaction. In mesophyll cells, the BiFC YFP signal of RH3-AGO2 aligned with the RFP-HDEL signal adjacent to the chloroplast periphery (Fig. 3e and Supplementary Fig. 8c). By imaging multiple focal planes within the same cell, we discovered that the BiFC YFP signal of RH3-AGO2 was present only at subdomains of the chloroplast periphery covered by the ER (marked by RFP-HDEL), and absent at regions of the chloroplast periphery not linked to the ER (Fig. 3e, upper panel and Supplementary Fig. 8e). Furthermore, the distance-intensity profile provided additional evidence for the association of the RH3-AGO2 interaction with the ER (Fig. 3f and Supplementary Fig. 8d).

To eliminate optical interference caused by clustered chloroplasts[43], the interaction signals of AGO2 and RH3 were further observed in epidermal cells containing very few chloroplasts. In these cells, the interaction signals of AGO2 and RH3 aligned perfectly with ER wrapping the chloroplast surface, while TOC64-III[44], an outer-membrane chloroplast protein, showed no colocalization with ER on certain chloroplasts (Fig. 3g). Furthermore, Z-stack scanning revealed

that the appearance and intensity of the RH3−AGO2 BiFC signal corresponded to the RFP−HDEL signal at the chloroplast periphery (Supplementary Movie 1). By contrast, TOC64-III−CFP distribution and intensity were independent of RFP−HDEL (Supplementary Movie 2).

The 6K2 protein of TuMV has been reported to associate with ER-like membranes, localizing at the chloroplast periphery[45–47]. To mimic the interaction between RH3 and AGO2 under physiological conditions, *pRH3::RH3-cYFP* and *pAGO2::nYFP-HA-AGO2* were expressed in Arabidopsis seedling. The resulting interaction signal (YFP) co-localized with TuMV-6K2-mCherry at the chloroplast periphery (Fig. 3h and Supplementary Fig. 9). These findings collectively support conclusion that RH3 interacts with AGO2 at ER−chloroplast MCSs.

RH3-AGO2 interaction promotes the loading of sRNAs

The interaction between RH3 and AGO2 suggests that RH3 may affect RNA silencing mediated by AGO2-associated sRNAs. To investigate the effect of RH3 on AGO2-associated sRNAs, we compared the sRNA profiles of Col-0 and *rh3* mutant plants. Since the *rh3* null mutant is embryonic lethality[48] and *amiR-RH3* knockdown seedlings display a
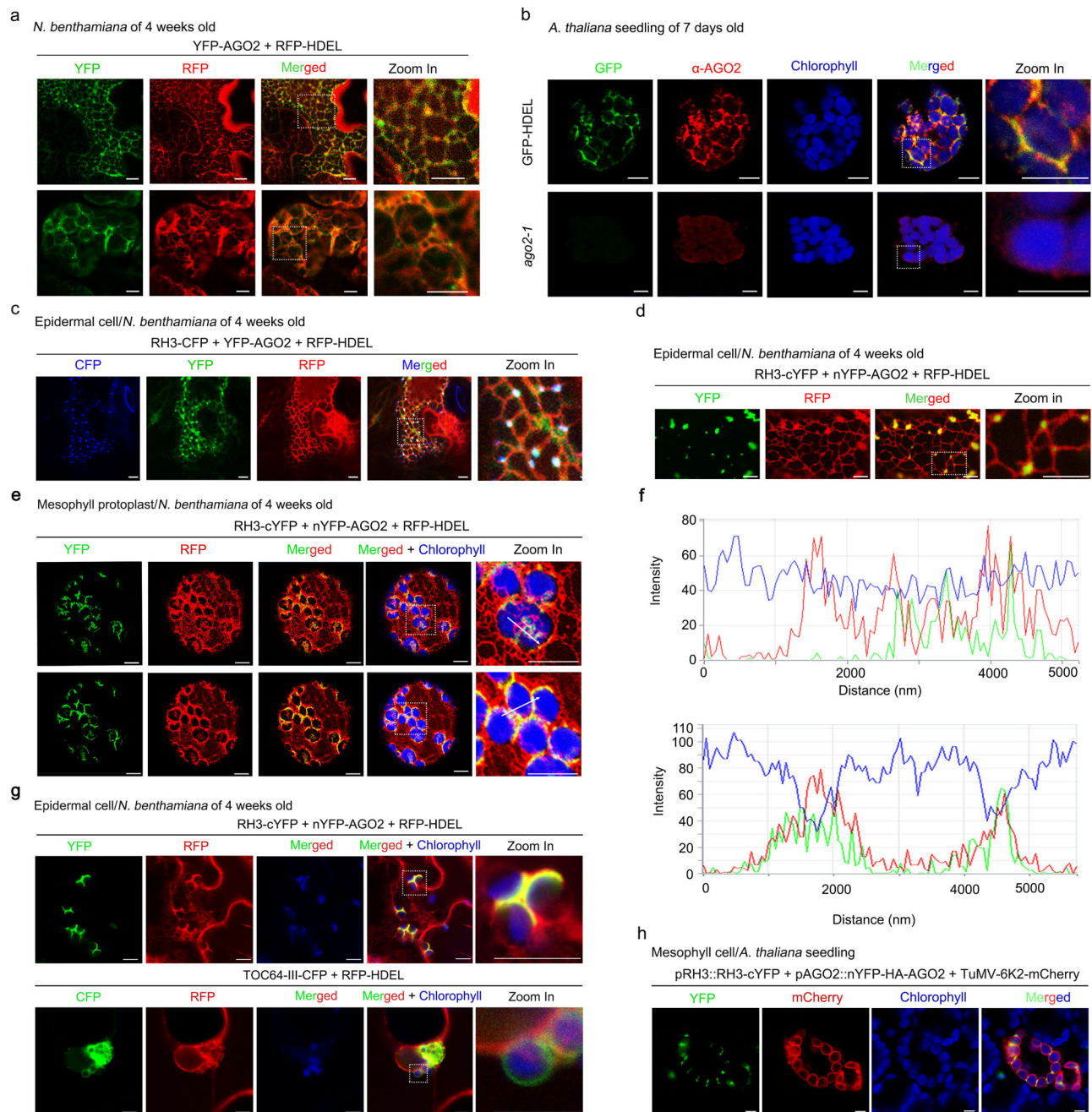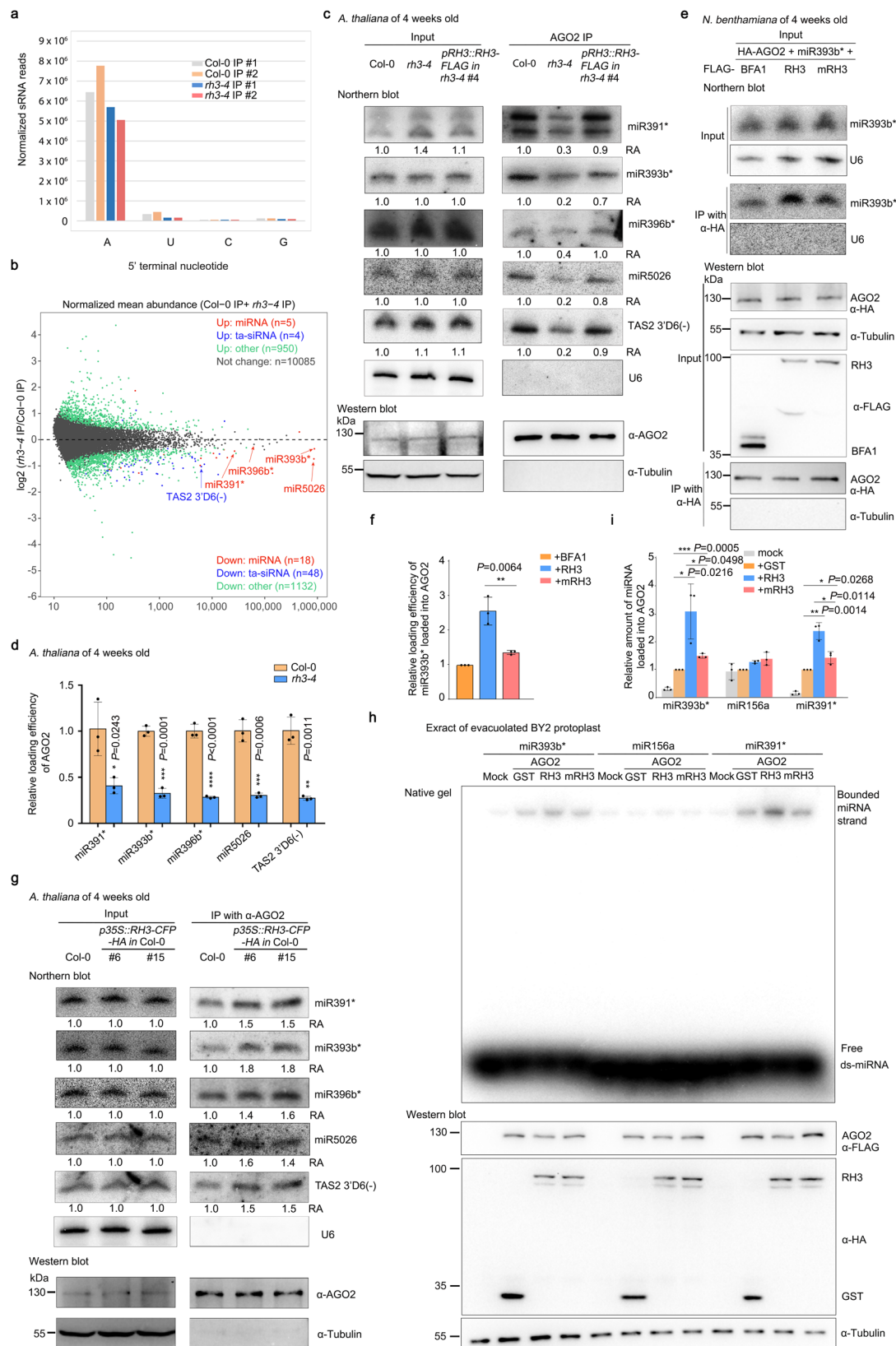
Fig. 3 | RH3 interacts with AGO2 at ER-chloroplast MCSs. a Microscopy analysis of the subcellular localization of AGO2 along the ER in *N. benthamiana* epidermal cells (upper panel) and mesophyll cells (bottom panel). AGO2 was labeled with YFP, which appear green. The ER was labeled with RFP-tagged HDEL, which appears red. **b** Immunofluorescence analysis of the localization of AGO2 along the ER in *p35S::GFP-HDEL* plant. AGO2 was labeled with anti-AGO2 antibody (red). The images of Z-axis scan was shown in Supplementary Fig. 8b. **c** Colocalization of RH3 and AGO2 on the ER of *N. benthamiana* epidermal cells. **d** BiFC analysis showing the interaction of RH3 with AGO2 along the ER in *N. benthamiana* epidermal cells. Reconstituted YFP fluorescence (green) and RFP-tagged HDEL (red) signals were observed. **e** BiFC analysis of the interaction of RH3 with AGO2 along the ER in *N. benthamiana* mesophyll protoplasts. Protoplasts of *N. benthamiana* expressing

RH3-cYFP and nYFP-AGO2 were extracted and was performed with different layer scanning. In the upper panel, AGO2 and RH3 interact specifically at loci covered with ER (red). In the bottom panel, the interaction signal (yellow) extends along ER (red). **f** Intensity profiles of colocalized AGO2 and RH3 (green), ER (red), and Chloroplast (Blue) corresponding to the region marked with white arrows in (**e**). The upper panel corresponds to the upper panel of (**e**), while the bottom panel corresponds to the bottom panel of (**e**). **g** BiFC analysis showing the interaction of RH3 with AGO2 along the ER in *N. benthamiana* epidermal cells. **h** The interaction site of RH3 and AGO2 co-localized with TuMV-6K2 at the chloroplast periphery in *A. thaliana* seedling. RH3-cYFP and nYFP-AGO2 were driven by native promotors. Controls are shown in Supplementary Fig. 9. Scale bar: **a**, **b**, **d**, and **e**, 5μm; **c**, **g** and **h**, 10 μm. These experiments were repeated three times, yielding similar results.

pale-green phenotype and growth cessation (Supplementary Fig. 10a), we utilized the *rh3-4* weak allele[48] (Supplementary Fig. 10b, c) for deep sequencing analysis of sRNAs. AGO2 is known to predominantly associate with 21-nt sRNAs starting with a 5′-A[12]. While the total 21-nt sRNAs (Supplementary Fig. 10d) and 21-nt sRNAs starting with a 5′-A

(Supplementary Fig. 10e) were comparable between *rh3-4* and Col-0 plants, the deep sequencing analysis of AGO2-bound sRNAs revealed that *rh3-4* plants had fewer sRNAs loaded into AGO2 compared to Col-0 plants (Fig. 4a, Supplementary Fig. 10f and Supplementary Data 2). These sRNAs included miRNAs, miRNA*s, and ta-siRNAs (Fig. 4b and

6

To further investigate the role of RH3 in AGO2 loading, we examined the subcellular localization of sRNAs associated with AGO2 using a FISH assay in Col-0 plants. The results revealed punctate compartments with a miR393b* signal at the periphery of chloroplasts (Supplementary Fig. 11). RNA immunoprecipitation (RIP)-qPCR using an anti-AGO2 antibody on isolated microsomal membranes (which are

Supplementary Data 2). Northern blot analysis confirmed that the levels of AGO2-loaded sRNAs were decreased in the *rh3-4* plants compared to Col-0 plants (Fig. 4c). Moreover when transgenic lines carrying *pRH3::RH3-FLAG* in the *rh3-4* background (Supplementary Fig. 10g, h) were generated, the sRNAs associated with AGO2 in these lines were comparable to those in Col-0 plants (Fig. 4c).

Fig. 4 | RH3-AGO2 interaction promotes the loading of sRNAs. a Relative frequency of 5′ terminal nucleotides in sRNAs bound to AGO2 in Col-0 and *rh3-4* plants. **b** Plot showing the mean abundance of AGO2-bound sRNAs in *rh3-4* plants compared with that in Col-0 plants. The 21-nt and 22-nt sRNAs with a mean number of reads >10 are shown. Data averaged from 2 biological replicates. **c** Northern blots display the accumulation of total sRNAs and AGO2-bound sRNAs in Col-0, *rh3-4*, and *pRH3::RH3-FLAG in rh3-4* transgenic plants. U6 and Tubulin served as the sRNA and protein loading control, respectively. **d** Deficiency in *RH3* significantly attenuates the loading of sRNAs into AGO2 in microsomes. The loading efficiency of AGO2 was calculated based on the RT-qPCR result shown in Supplementary Fig. 12e. The error bars indicate mean ± SD (*n* = 3 biologically replicates with averaged technical duplicates shown), and *p* values determined by two-tailed Student's *t* test. **e, f** The interaction of RH3 with AGO2 facilitates the loading of miR393b* into AGO2 in *N. benthamiana*. Quantification of miR393b* associated with AGO2 based on 3

biological replicates is shown in (**f**). The error bars indicate mean ± SD, and *p* values determined by two-tailed Student's *t* test. **g** Northern blots showing the accumulation of total and AGO2-bound sRNAs in Col-0 and *p35S::RH3-CFP-HA in* Col-0 transgenic plants. **h** RH3 promotes the association of miR393b* and miR391* with AGO2 in vitro. AGO2 bound miR393b* or miR391* complexes, with increased electrophoretic mobility, were retained at the top of the gel and separated from free miRNA duplexes. Loading of miR156a/miR156a* into AGO2 was determined as the negative control. **i** Relative **i**ncrease of miRNA loaded into AGO2 in the presence ('RH3') or absence ('GST/mRH3') of wild type RH3 protein. Data were shown as relative amounts of miRNA loaded into AGO2 normalizing to in vitro system expressing GST and AGO2 protein. Errors bars are mean ± SD of 3 biological replicates. Two-tailed student's *t* test was performed to determine statistical significances of two groups. *, *P* < 0.05, **, *P* < 0.01, ***, *P* < 0.001. Source data are provided as a Source Data file.

enriched for the ER network) showed that the loading efficiency of sRNAs into AGO2 was significantly higher in the microsomal membrane fraction compared to the soluble fraction (Supplementary Fig. 12a–c). With Col-0 and *rh3-4* plants, microsomal membrane fractions and immunoprecipitation assays revealed that the presence of RH3 and AGO2 in the microsomal membrane fractions and the levels of AGO2-loaded sRNAs in the *rh3-4* microsomal membrane fraction were significantly lower compared to those in the Col-0 microsomal membrane fraction (Fig. 4d, and Supplementary Fig. 12d–f). These findings suggest that ER–chloroplast MCSs may serve as sites for the loading of sRNAs into AGO2 and further demonstrate that RH3 facilitates the loading of sRNAs into AGO2.

To investigate whether the effect of RH3 on sRNA loading into AGO2 is related to the abnormal chloroplast morphology[49], we performed experiments using *N. benthamiana* plants coexpressing HA-AGO2 and pre-miR393b with *p35S::RH3-FLAG*. We observed a significant improvement in the binding of miR393b* to AGO2 in the presence of transient expressed RH3 (Fig. 4e, f), although the chloroplast morphology was similar between samples (Supplementary Fig. 13a). Further analysis with the *p35S::RH3-CFP-HA in* Col-0 *Arabidopsis* plants showed that sRNAs associated with AGO2 were more abundant in the *RH3*-overexpressing plants than those in the Col-0 plants (Fig. 3g and Supplementary Fig. 13b). Notably, the *p35S::RH3-CFP-HA in* Col-0 transgenic plants did not display any obvious developmental defects (Supplementary Fig. 13c), and the chloroplast structures appeared normal (Supplementary Fig. 13d). These findings suggest that the role of RH3 in promoting sRNAs loading into AGO2 does not result from abnormal chloroplast morphology.

RH3 may indirectly inhibit the degradation of primary miRNA (pri-miRNA) via the retrograde signaling pathway[50]. However, we observed that the accumulation of tested pre- and pri-miRNAs, as well as *TAS2*, in the *rh3-4* mutant plants, was not significantly altered (Supplementary Fig. 13e–g). To further test this hypothesis, we performed in vitro loading assays (Supplementary Fig. 14a). The AGO2 protein, synthesized in a wheat germ extract system, was mixed with RH3 or GST proteins that was translated in an extract of evacuolated BY-2 protoplasts[51] to perform in vitro loading assays. The loading of miR393b/miR393b*, miR391/miR391* or miR156a/miR156a* into AGO2 were determined (Supplementary Fig. 14b, c). As expected, miR393b* and miR391*, but not miR156a were associated with AGO2. Moreover, the association of miR393b* and miR391* with AGO2 was significantly promoted by RH3 (Fig. 4h, i). GST was used as control of RH3. Since the BYL extract does not contain intact chloroplasts required for the retrograde signaling, the in vitro loading assays together with the unchanged levels of pri-/pre-miRNA demonstrate that RH3 does not promotes the level of sRNAs loaded into AGO2 through retrograde signaling.

To determine whether RH3 promotes the loading of sRNAs into AGO2 by its interaction with AGO2, mRH3 with reduced interaction with AGO2 (Fig. 1d–g) was used. Coexpression of HA-AGO2 and pre-miR393b

with wild-type RH3 or mRH3 in *N. benthamiana* plants showed that the accumulation of miR393b* bound to AGO2 was higher in plants coexpressing wild-type RH3 compared to those coexpressing mRH3 (Fig. 4e, f). This result was further confirmed in the in vitro loading assays (Fig. 4h, i). The mutant form of RH3 with impaired interaction indeed affected its ability to facilitate sRNA loading into AGO2.

Furthermore, the decreased loading of sRNAs into AGO2 in the *rh3* mutant plants had functional consequences. The *rh3-4* mutant plants exhibited higher accumulation of the MEMB12 protein, a target of miR393b* involved in the secretion of the PR1 protein[12] (Supplementary Fig. 15a). Additionally, upon treatment with a bacterial pathogen, the secretion of PR1 protein was decreased in the *rh3-4* mutant plants compared to Col-0 plants (Supplementary Fig. 15b, c). Moreover, the transcripts of *At1g28490* and *At5g14180*, which are predicted targets of miR5026[52], were higher in *rh3-4* mutant plants compared to Col-0 plants (Supplementary Fig. 15d). These findings further demonstrate the role of RH3 in promoting the functions of sRNAs bound to AGO2.

The RH3-AGO2 interaction at ER–chloroplast MCSs facilitates the loading of exogenous vsiRNAs into AGO2

Turnip yellow mosaic virus (TYMV), *Turnip mosaic virus* and other similar viruses, which are threats to crops and vegetables, have been shown to perform their replication processes at the chloroplast periphery[53–55]. These viruses manipulate host membranes and modify the chloroplast membrane structure to facilitate their replication processes[56,57]. During TYMV infection, there is a rearrangement of ER structures over viral vesicles, followed by the formation of chloroplast clumps surrounding these vesicles[53,58]. These studies suggested that ER-chloroplast MCSs might be the active sites for the replication of TYMV and some other viruses. The 140K proteins of TYMV, which are required for the TYMV RNA replication, localizes to the chloroplast periphery[58–60]. By coexpressing CFP-HDEL (ER) and *dsRed-TYMV::140 K* in *A. thaliana* seedling, we find that the replication complex of TYMV (*dsRed-TYMV::140K*) indeed associates with ER (Supplementary Fig. 16a). Additionally, the RH3-AGO2 interaction site co-localizes with 140K protein of TYMV at the chloroplast periphery (Supplementary Fig. 16b). We then infected *A. thaliana* seedling with *dsRed-TYMV::140K* and coexpressed nYFP-AGO2, RH3-cYFP, and CFP-HDEL. The results demonstrated the colocalization of the *dsRed-TYMV::140K* viral marker with the signals from CFP-HDEL (ER) and YFP (RH3-cYFP/nYFP-AGO2) (Fig. 5a). Moreover, RNA-fluorescence in situ hybridization assays revealed the localization of the replication intermediates of TYMV (TYMV dsRNA) at the chloroplast periphery, the majority of which co-localized with the RH3-AGO2 interaction site (Fig. 5b, Supplementary Fig. 16c). The accumulation of dsRNA at ER-chloroplast MCSs may activate RNA silencing-mediated plant resistances to viruses. Indeed, DCL4, responsible for processing viral dsRNAs[61] (Supplementary Fig. 16d), and RNA-dependent RNA polymerase 6 (RDR6), which amplifies viral vsiRNAs[62], were scattered around the chloroplast periphery (Supplementary Fig. 16d). These findings
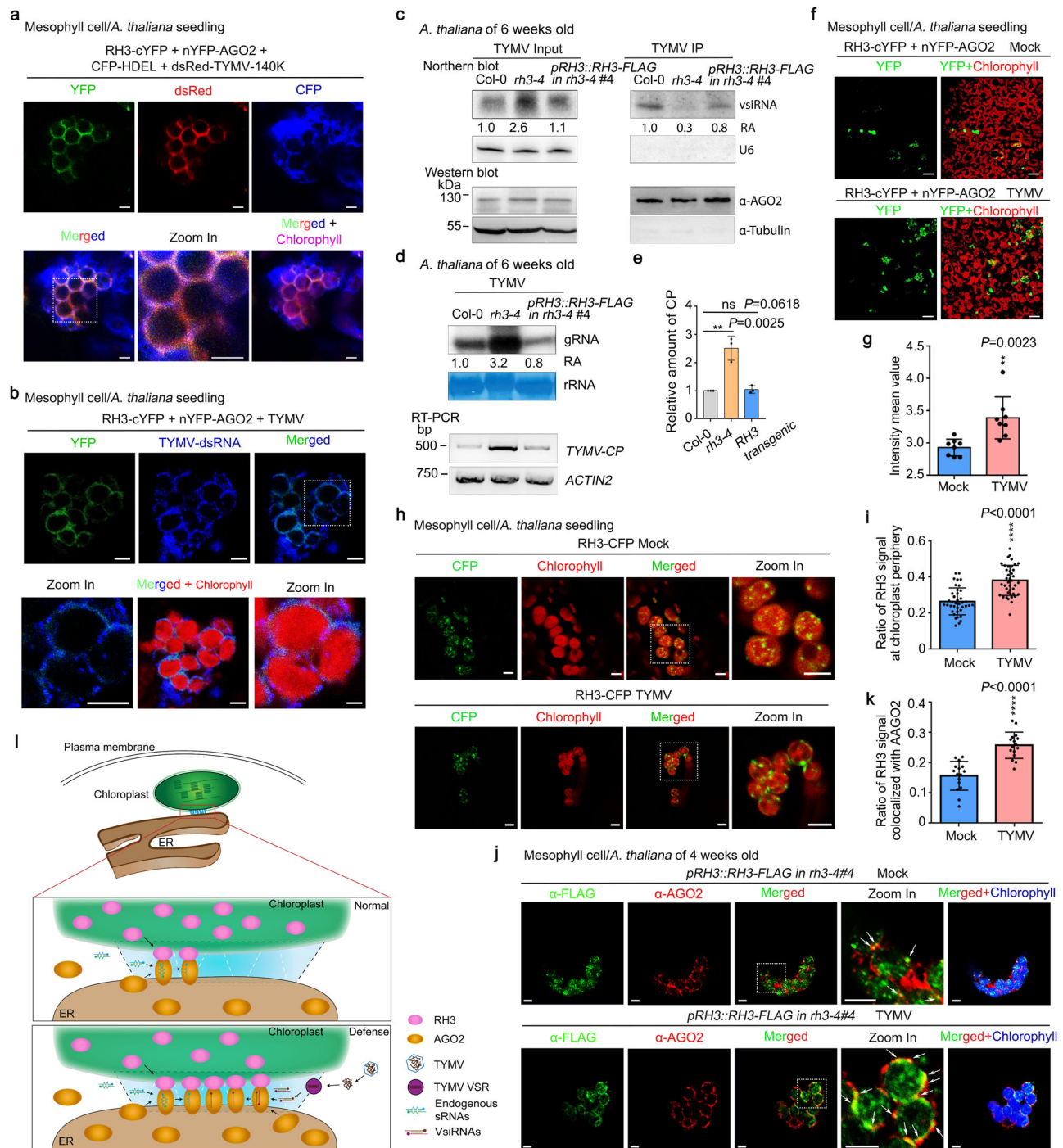
Fig. 5 | RH3-AGO2 interaction co-localizes with viral replication at ER–chloroplast MCSs. a Colocalization of the TYMV 140K protein with RH3-AGO2 interaction sites at ER–chloroplast MCSs. **b** Localization of TYMV dsRNAs at RH3-AGO2 interaction sites at the chloroplast periphery. P19 was added to trigger the accumulation of TYMV dsRNA. Controls for (**b**) were shown in Supplementary Fig. 16c. **c** RH3 enhanced the loading of TYMV vsiRNAs into AGO2. IP was conducted using anti-AGO2 antibody. **d, e** RH3 enhanced plant immunity to TYMV. **d** The accumulation of TYMV genomic RNAs increased (upper panels) and CP transcript level increased (bottom panels) in *rh3-4* plants. Quantitative data from 3 replicates are shown in (**e**). **f-g** BiFC assays demonstrating increased interaction between RH3 and AGO2 upon viral infection. YFP signals of 8 sets of pictures were quantified with Zen software and plotted in (**g**). **h, i** Microscopy analysis of the subcellular localization of RH3 in *A. thaliana* seedling with or without viral infection. The ratio of RH3-CFP punctate compartments at chloroplast periphery was calculated and

indicated on the right (**i**). *n* = 39. **j, k** Immunofluorescence analysis of the colocalization of AGO2 and RH3 with or without viral infection in fixed *pRH3:RH3-FLAG in rh3-4* cells. Arrows indicate colocalization sites. The ratio of RH3 colocalized with AGO2 to the total RH3 level is shown in (**k**). *n* = 16. **l** A model illustrating that RH3 promotes the sRNA loading into AGO2 at ER–chloroplast MCSs. RH3 interacts with AGO2 at ER–chloroplast MCSs, facilitating the loading of sRNAs into AGO2 at these sites. The replication site of viruses such as TYMV overlaps with AGO2-RH3 interaction site. Viral infection increases the interaction of RH3 and AGO2. The increased RH3-AGO2 interaction promotes the loading of vsiRNAs into AGO2, enhancing plant antiviral defense. Scale bar: **a, b, h** and **j**, 5μm; **f**, 20 μm. The experiments producing **a, b** and **c** were repeated three times, yielding similar results. The error bars in **e, g, i** and **k** indicate mean ± SD, and *p* values present on the figure were determined by two-tailed Student's *t* test. Source data are provided as a Source Data file.

provide evidence that the TYMV replication may associate with RNA silencing at ER–chloroplast MCSs.

Roles of RH3 on sRNAs loading into AGO2 led us to investigate whether RH3 also facilities the loading of vsiRNAs into AGO2. The levels of vsiRNAs loaded into AGO2 in TYMV-infected Col-0, *rh3-4*, and *pRH3::RH3-FLAG in rh3-4* plants were thus measured. Although the total vsiRNA levels in the *rh3-4* mutant plants were higher than those in the Col-0 plants, the levels of vsiRNAs loaded into AGO2 were significantly reduced in the *rh3-4* mutant plants (Fig. 5c). The levels in *pRH3::RH3-FLAG in rh3-4* were comparable to those in Col-0 plants (Fig. 5c). These observations suggest that RH3 facilitates the loading of vsiRNAs into AGO2.

AGO2 has been shown to play a significant role in plant resistance to viruses[13–17]. A previous study demonstrated that AGO2 contributes to limiting the TYMV infections[63]. To investigate whether RH3 promotes plant antiviral immunity, the susceptibility of *rh3-4* plants to TYMV was examined. Indeed, the viral genomic RNA and the RNA transcript of viral coat protein (CP) in systemically infected leaves of *rh3-4* plants was increased compared to that in Col-0 or *pRH3::RH3-FLAG in rh3-4* plants (Fig. 5d, e).

In response to viral infection, more RH3 is located to the chloroplast periphery to interact with AGO2. A BiFC assay conducted in TYMV-infected *A. thaliana* seedlings showed an increased YFP signal compared to the control plants (Fig. 5f, g), while the levels of AGO2 and RH3 protein were not significantly increased (Supplementary Fig. 16e). Additionally, an elevated RH3-CFP signal at the chloroplast periphery were observed in TYMV-infected samples (Fig. 5h, i). Immunofluorescence assays also showed increased colocalization between RH3 and AGO2 in TYMV-infected samples (Fig. 5j, k). These findings suggest that viral infection causes the relocation of RH3 to the chloroplast periphery, where it interacts with AGO2 and enhances the loading of sRNAs into AGO2.

To investigate the dependence of the antiviral effects of RH3 on AGO2, a *rh3-4/ago2-1* double mutant was generated (Supplementary Fig. 17a, b) and infected with TYMV. Intriguingly, TYMV caused more severe disease symptoms in the *rh3-4/ago2-1* plants (Supplementary Fig. 17c), and the accumulation of TYMV genomic RNAs was more abundant in the *rh3-4/ago2-1* plants (Supplementary Fig. 17d). These results suggest that while RH3 promotes plant antiviral immunity, it does not solely depend on AGO2.

In addition to AGO2, other AGO proteins, such as AGO7, have been shown to participate in plant immune responses against viruses[3,64,65]. RH3 may promote antiviral immunity by facilitating the loading of sRNA loading into AGO7 and other AGOs in addition to AGO2. Co-localization and interaction studies demonstrated that RH3 partially colocalized with AGO7 at the chloroplast periphery (Supplementary Fig. 18a) and interacted with AGO7 (Supplementary Fig. 18b). Moreover, RH3 was found to facilitate the loading of miR390 into AGO7 (Supplementary Fig. 18c). Interestingly, RH3 did not show a similar effect on the loading and regulation function of tested sRNAs associated with AGO1, but promoted the association of siRNA AtREP2 with AGO4 (Supplementary Fig. 18d–g). These findings indicate that RH3 may play a role in facilitating the loading of sRNAs into multiple AGO proteins.

Discussion

This study has revealed an important connection between viral replication and RNA silencing-mediated antiviral defense mechanisms in plants. It demonstrates that ER-chloroplast MCSs serve as sites for both the loading of sRNAs into AGO2 (Fig. 5l, middle panel) and viral replication (Fig. 5l, bottom panel). The RH3 protein is found to facilitate the loading of sRNAs into AGO2 at these sites. Furthermore, viral infections enhance the association of RH3 with AGO2, leading to increased loading of vsiRNAs into AGO2 and enhanced plant resistance to viruses.

Previous studies have highlighted the roles of the ER in RNA silencing, with AGO1, a peripheral membrane protein[66,67], being localized to the ER and the translation inhibitions of miRNA targets in ER-associated membrane-bound polysomes[26]. In our study, we observed sRNAs and major RNA silencing components, including DCL, RDR, and AGOs, at the chloroplast periphery/ER-chloroplast MCSs. The loading of sRNAs into AGO2 was found to occur at these MCSs, and RH3 interacts with and facilitates the loading of AGO2 at these sites. AGO7 was found to associate with membranes that are coeluted with calnexin, a resident ER protein[68]. Moreover, AGO7 tightly interacts with miR390 and stalls the MBPs bound to *TAS3* transcripts[25,68,69], indicating that AGO7 localizes to the ER to cleave *TAS3* transcripts. Additionally, approximately 60% of AGO7 colocalizes with the 6K2 protein of TEV in the cytoplasm[68]. Notably, our results show that the TYMV 140K protein localizes at ER–chloroplast MCSs. RH3 also colocalizes with AGO7 at the chloroplast periphery and promotes the loading of miR390 into AGO7, suggesting that AGO7 may also load sRNAs at ER–chloroplast MCSs. Moreover, RH3 also promotes the loading of siRNA AtREP2 into AGO4. Therefore, ER-chloroplast MCSs may serve as important loading sites for sRNAs, and RH3 may has a broad role in facilitating their loading at these locations.

Chloroplast are sites for the synthesis of carbon, ATP, amino acids, purine, pyrimidine, salicylic acids, and jasmonic acids[54,55], which are required for the proliferation of viruses and host immune responses. Therefore, viruses target the chloroplast to eavesdrop cell compartments and membrane contents for their own proliferation[54], while simultaneously suppressing host immune responses. The ER is also a key site for the biosynthesis of proteins, lipids and other molecules that are also required for the proliferation of viruses[70]. Many plant viruses remodel and use ER or ER-derived vesicles for viral proliferation[71,72]. As MCSs contain molecules from two opposing organelles that may be required for viral proliferation, viruses may exploit host MCSs as centres to fulfill their proliferations[73,74]. For example, the movement protein of *Turnip vein clearing virus* interacts with synaptotagmin SYTA, a protein enriched at ER–plasma MCSs, remodeling ER–plasma MCSs at plasmodesmata to form viral replication sites[75]. Additionally, VAP27-1, another protein enriched at ER–plasma MCSs, also interacts with viral proteins and facilitates viral replication[76,77]. Our study demonstrated that the replication of TYMV takes place at ER–chloroplast MCSs, emphasizing the importance of these sites in viral proliferation.

To efficiently inhibit viral replication, RNA silencing-mediated antiviral immunity may cytobiologically connect with viral replication sites such as ER-chloroplast MCSs. AGO2 and other AGO proteins, the central protein of RNA silencing, associate with vsiRNAs and play pivotal roles in plant resistances to viruses[3,15–18,64,78]. To efficiently inhibit viral proliferation, AGOs need to be in the right place upon the infection of viruses[19]. Our study found that viral replications co-localize with RH3-AGO2 interaction sites at ER-chloroplast MCSs. AGO7 also plays important roles in plant resistance to viruses[65]. As RH3 colocalizes with AGO7 at the chloroplast periphery and facilitates the loading of sRNAs into AGO7, AGO7 may also load vsiRNAs at these sites. Therefore, ER–chloroplast MCS provides a space not only for viral replication and loading of endogenous sRNAs but also for the loading and potential action of vsiRNA-RISCs, establishing a cytobiological link between viral replication and RNA silencing.

It is worth noting that same AGOs may load different types of sRNAs at different locations within the cell. For example, miRNAs are typically loaded into AGO1 in nuclei, while phasiRNAs are loaded into AGO1 in the cytoplasm[8]. Intriguingly, some unloaded mature miRNAs or miRNA/miRNA* duplexes have been found to accumulate in the cytoplasm, suggesting that the loading of the portion of specific miRNAs into AGO1 may also occur in the cytoplasm[79]. Indeed, mobile miRNAs are reported to load into AGO1 in the cytoplasm[80]. AGO2, on the other hand, not only loads miRNAs, miRNA*s, and vsiRNAs, but it

also associates with diRNAs and participates in repairing double-strand breaks in the nucleus[11]. Therefore, AGO2 may also have multiple subcellular localizations for sRNA loading.

In conclusion, this study uncovers the cytobiological connections between viral replication, RNA silencing, and plant antiviral defense mechanisms. ER tubules are present throughout the cytosol and form various MCSs with multiple organelles[20,24,81–83]. Other organelles such as endosomes, lysosomes, peroxisomes, and mitochondria have also been suggested as replication sites for various plant viruses[46,56], and it is worth investigating roles of other ER–organelle MCSs in viral replications and RNA silencing.

Methods

Plant materials

Arabidopsis thaliana T-DNA insertion lines *rh3-4* (SALK_005920)[49] were obtained from the Arabidopsis Biological Resource Center. The *rh3-4* line was crossed with *ago2-1* (SALK_003380) to generate homozygous *rh3-4/ago2-1* double mutant. The *ago2-1* mutant and *pAGO2::HA-AGO2 in ago2-1* were previously described[12]. *Arabidopsis* transgenic plant expressing *RH3* under *35S* promoter were generated by *Agrobacterium tumefaciens* (*A. tumefaciens*)-mediated flower dipping transformation in both Col-0 and *rh3-4* backgrounds[84]. Transformants were selected on 1/2 Murashige and Skoog (1/2 MS) agar plates supplemented with 0.1% basta to get *p35S::RH3-CFP-HA in* Col-0 and *p35S::RH3-CFP-HA in rh3-4* plants. The *p35S::amiR-RH3* construct was transformed into Col-0 to obtain *amiR-RH3* transgenic plants. The *pRH3::RH3-FLAG* construct was transformed into *rh3-4* to obtain *pRH3::RH3-FLAG in rh3-4* transgenic plants. The *p35S::3HA-GFP in* Col-0 was previously described[85].

Typically, 4-week-old *Arabidopsis* plants were used for various assays. Due to the serious developmental defects, *p35S::amiR-RH3 in* Col-0 plant was not used in further experiment. The phenotype of *p35S::amiR-RH3 in* Col-0 T0 lines were shown. The T2 generations of stable transgenic lines were used for subsequent experiments. For viral infections, 4-week-old *Arabidopsis* plants were used for virus infection and the systemic leaves were harvested at 14 dpi for TYMV. 4-week-old *N. benthamiana* plants were used for viral infection and transient expression, and the inoculated leaves were harvested at 3 dpi. Protoplasts from 2-week-old *Arabidopsis* plants were used for transient expression in protoplasts. Adult plants were grown in a greenhouse at 22 °C ± 1 °C under a 12 h light/12 h dark cycle, while seedlings were grown on 1/2 MS plates in a growth chamber (22°C, 12 h light/12 h dark cycle). Additional details for individual experiments are provided in the figure legends. *N. benthamiana* wild-type plants were grown in a greenhouse at 22°C ± 1°C under 12 h light/12 h dark photoperiod. P19, an RNA silencing suppressor, was not included in transient expression experiments unless otherwise notified.

Plasmids and cloning procedures

To generate *pENTR* constructs, the coding sequences of *RH3, AGO2, BFA1, Calnexin* (*CNX*), *AGO7, DCL4* and *TOC64-III* were amplified from cDNA derived from Col-0 plants. For Co-IP assays, the coding sequence of *RH3, BFA1, AGO2,* and *AGO7* were recombined from *pENTR* vectors into *pFH* or *pMDC32* vector using Gateway LR Clonase II Enzyme Mix (Invitrogen), resulting in the generation of *p35S::RH3-FLAG, p35S::BFA1-FLAG, p35S::HA-AGO2,* and *p35S::HA-AGO7* constructs[86–88]. For transient expression assay, the coding sequence of *RH3, AGO2, AGO7, DCL4* and *TOC64-III* were recombined from *pENTR* vectors into *pEarleyGate-102, pEarleyGate-104* or *pBI121-RFP* by Gateway LR Clonase II Enzyme Mix (Invitrogen), resulting in the generation of *p35S::RH3-CFP-HA, p35S::YFP-AGO2, p35S::YFP-AGO7, p35S::DCL4-RFP,* and *p35S::TOC64-III-CFP-HA* constructs. dsRed-TYMV-140K vector was constructed by recombinant PCR to ligate *TYMV-140K* into *pGDR* vector using SoSoo cloning kit (Tsingke). For the BiFC assay, the coding sequence of *GST,*

RH3, BFA1, CNX and *AGO2* were recombined from *pENTR* vector into *pSITE-cEYFP-C1, pSITE-cEYFP-N1, pSITE-nEYFP-N1* or *pSITE-nEYFP-C1,* gateway-compatible BiFC vectors, using Gateway LR Clonase II Enzyme Mix (Invitrogen), resulting in the generation *p35S::GUS-cEYFP-C1, p35S::RH3-cEYFP-N1, p35S::BFA1-cEYFP-N1, p35S::CNX-nEYFP-N1,* and *p35S::nEYFP-AGO2-C1* constructs[89]. *pENTR-GUS* was provided by Gateway LR Clonase II Enzyme Mix (Invitrogen). *p35S::nEYFP* was constructed by inducing a stop codon in the region between *nEYFP* and AGO2 to *p35S::nEYFP-AGO2-C1* construct. *p35S::cEYFP* was constructed by inducing a stop codon in the region between *cEYFP* and GUS to *p35S::cEYFP-GUS-C1* construct. *p35S::DCL1-YFP* and *pEarleyGate100-MIR393b* were described previously[12,85]. For the generation of *pRH3::RH3-cEYFP,* a 3026 bp *RH3* promoter and *RH3* genomic DNA fragment was amplified from Col-0 genomic DNA, and a *cEYFP* fragment with stop codon was recombined to the C terminal of RH3 by recombination PCR. The RH3 promotor-RH3-cEYFP fragment was cloned into *pENTR* vector with pENTR™/SD/D-TOPO™ Cloning kit (Invitrogen) according to the manufacturer's instructions, and further ligated to pV73 vector using Gateway LR Clonase II Enzyme Mix (Invitrogen). Similarly, *pAGO2::HA-nEYFP-AGO2* was generated by recombining a 1576 bp native promotor with *HA-nEYFP-AGO2* and ligating into pCAMBIA 1305 vector using using ClonExpress Ultra One Step Cloning Kit (Vazyme). *p35S::RFP-HDEL, p35S::YFP-HDEL* and *p35S::CFP-HDEL*[42], *p35S::RDR6-RFP*[90] and *Mit-GFP, Nuc-GFP,* and *Chl-GFP*[40] were also described previously.

For prokaryotic expression, *RH3-HA* and *GST-HA* fragments were amplified with primers containing HA tag sequences using *pENTR-RH3* and *pENTR-GST* as templates. The amplified *RH3-HA* or *GST-HA* fragments were inserted into *pET-32a* and digested with *Nco*I and *Xho*I, resulting in the generation of *pET-32a-RH3-HA* and *pET-32a-GST-HA.* Codon-optimized *FLAG-AGO2* was synthesized (GenScript) and inserted into *pET-28a* digested with *Nde*I and *Sal*I. *RH3D70, RH3(1-250), RH3(251-500),* and *RH3(501-748)* were amplified from *pET-32a-RH3* using sets of primers: 5′ forward containing an *Nco*I digestion site and 3′ reverse primer containing HA tag sequence and *Xho*I digestion site, respectively. *RH3D70Δ(251-350), RH3D70Δ(351-450), RH3D70Δ(451-550), RH3D70Δ(551-650), RH3D70Δ(651-748), RH3D70Δ(451-500), RH3D70Δ(501-550), RH3D70Δ(651-700), RH3D70Δ(701-748), RH3D70 K459A R460A R463A R467A, RH3D70 E466A D468A E474A,* and *RH3D70 D483A E486A D490A* ligated *pET-32a* vectors were constructed by recombinant PCR followed by *Dpn*I digestion with *pET-32a-RH3D70* as template. *pET-32a-/pFH-RH3K459A R460A R463A R467A* (mRH3) were constructed by recombinant PCR followed by *Dpn*I digestion with *pET-32a-RH3* or *pFH-RH3* as template.

The *p35S::amiR-RH3* construct was generated by overlapping PCR using the pri-miR319a backbone and cloned into *pEarleyGate-100* as described previously[12]. A 6351 bp genomic DNA fragment containing the *RH3* promoter and coding sequence was amplified from Col-0 genomic DNA and cloned into *pENTR* vector with pENTR™/SD/D-TOPO™ Cloning kit (Invitrogen) according to the manufacturer's instructions. The 6351 bp fragment was then cloned into *pEarleyGate-302* using Gateway LR Clonase II Enzyme Mix (Invitrogen), resulting in the generation of *pRH3::RH3-FLAG* construct.

For in vivo protein expression-related clones, *RH3-HA* and *GST-HA* fragments were amplified with primers containing *SP6-TMVΩ* at 5′ end of *RH3/GST* as forward primer and 3′ *RH3/GST* with *HA* as reverse primer, and ligated to *pEASY-Blunt* vector. *FLAG-AGO2* was amplified with primers containing TMVΩ and FLAG at 5′ end of *AGO2* as forward primer and 3′ end of *AGO2* as reverse primer, and ligate to *pEASY-Blunt* vector. Further mutant PCR was done to remove the sequence between T7 promoter and PCR product, and the vectors were ligated in *E. coli*. These vectors are digested by *Bst*XI before performing transcription. All primers used for constructing these plasmids are listed in Supplementary Data 3.

Bacterial infection and PR1 protein extraction

Pseudomonas syringae pv. Tomato (*Pst*) DC3000 carrying the *avrRpt2* effector was cultured at 28°C in KB medium supplemented with 50 μg/ml rifampicin and 50 μg/ml kanamycin. Bacteria treatments were performed as previously described[12]. Briefly, 4-week-old plants were inoculated with *Pst* (*avrRpt2*) strain at a concentration of $OD_{600} = 0.02$. The infiltrated leaves were harvested at 12 h post-inoculation (hpi). Before collecting intercellular wash fluid (IWF), equal amounts of leaves from different plants were vacuumed with 20 mM phosphate buffer (KH_2PO_4 and K_2HPO_4, pH 7.4) for 10 min, as previously described[91]. The leaves were then centrifuged at 1,500 g for 5 min to collect IWF. The PR1 protein in the total and intercellular fluid was examined using α-PR1 polyclonal rabbit antibody (1:4,000)[12], with Tubulin serving as a loading control.

Viral infection

The *A. tumefaciens* strain GV3101 carrying the genome of TYMV[60] was cultured at 28°C in LB medium supplemented with 25 μg/ml rifampicin, 50 μg/ml gentamicin, and 25 μg/ml kanamycin. The inoculations of TYMV were performed as described[53,92]. Briefly, the *A. tumefaciens* GV3101 carrying TYMV constructs were resuspended with buffer [10 mM $MgCl_2$, 0.15 mM Acetosyringone (AS), and 10 mM 2-Morpholinoethanesulfonic Acid (MES)] to a final concentration of $OD_{600} = 0.5$, respectively. For virus inoculation, 4-week-old *A. thaliana* plants were used, and systemic tissues were harvested at 14 dpi for protein and RNA analyses, as detailed in the "Plant material" section. For transient expression in *A. thaliana* seedling, 3-day-old Col-0 WT were used for virus inoculation and performed as previously described[93], and the inoculated leaves were collected at 4-5 dpi for fluorescence microscopy or Western blot analysis.

Transient expression in Arabidopsis seedling

The transient expression of *p35S::CFP-HEDL*, *p35S::RH3-cYFP*, *p35S::nYFP-AGO2*, *pRH3::RH3-cEYFP*, *pAGO2::HA-nEYFP-AGO2* and *p35S::dsRed-TYMV-140K* in Arabidopsis seedling were performed as previously described[93]. Briefly, the *A. tumefaciens* GV3101 carrying target construct were resuspended with buffer [5% sucrose, 0.2 mM AS, and 10 mM MES] to a final concentration of $OD_{600} = 2.0$, respectively, and used to infiltrate 3-day-old Col-0 WT. The infiltrated plants were cultured for 3-5 days before being used for further experiments.

Protoplast isolation and transfection

Protoplasts were isolated as previously described[94]. Briefly, leaves from 4-week-old plants were cut into 0.5-1 mm strips with razor blades. The leaf strips were then incubated in enzyme solution [1.5% cellulase R10, 0.4% macerozyme R10, 0.4 M mannitol, 20 mM KCl, 20 mM MES (pH 5.7), 10 mM $CaCl_2$, 0.1% BSA] in dark for 4 h with gentle shaking (40 rpm) at 37 °C. The resulting protoplasts were filtered and washed with the equal volume of pre-cold W5 solution [154 mM NaCl, 125 mM $CaCl_2$, 5 mM KCl, and 2 mM MES (pH 5.7)] for three times. After centrifugation at 100 g for 2 min at 4 °C, the protoplasts were suspended in pre-cold W5 solution and incubated on ice for 30 min.

For PEG-mediated transfection, the protoplasts were resuspended in MMG solution [(0.4 M mannitol, 15 mM $MgCl_2$, 4 mM MES (pH 5.7)]. The transfection was performed by gently mixing 200 μl protoplasts with the desired construct (20 μg) and 220 μl PEG solution (40% PEG4000, 100 mM $CaCl_2$, 0.2 M mannitol) for 10 min at room temperature. The transfected protoplasts were then washed three times with W5 solution. After the washing steps, the transfected protoplasts were suspended with 1 ml W5 solution and cultured under white light at room temperature. CFP/GFP fluorescence in transfected protoplasts was observed 10 to 15 h after transfection using the confocal microscope. *N. benthamiana* protoplasts used for transient protein expression were imaged directly without transfection.

Microsome isolation

To isolate microsomes for determining the association of RH3 and AGO2 with the ER, the following procedure was performed with minor modifications[25]. First, 2 g of seedlings were ground in 5 ml microsome isolation buffer [100 mM Tris-HCl (pH 7.5), 5 mM EGTA, 15 mM $MgCl_2$, 5 mM DTT, 0.3 M sucrose, and a tablet of cOmplete proteinase inhibitor per 50 ml] at 4 °C. The resulting cell lysate was filtered through two layers of miracloth, and a 100 μl aliquot was taken as the total proteins. Next, the cell lysate was centrifuged at 8000 g for 5 min twice to remove debris, resulting in the isolation of the cytosolic proteins. The soluble fraction resulting in the isolation was then performed ultracentrifugation for 30 min at 100,000 g, 4 °C. The resulting supernatant was collected for further Western blot assays and labeled as the "supernatant" fraction. The pellet obtained after ultracentrifugation was suspended in 5 ml isolation buffer, and applied onto a sucrose gradient (2.5 ml 20% sucrose/2.5 ml 60% sucrose). The sucrose gradient was then centrifuged at 100,000 g for 1 h at 4 °C. Microsomes were recovered from the interface between the two sucrose layers and precipitated by centrifugation at 100,000 g for 30 min at 4 °C.

For the isolation of microsomes for AGO2 immunoprecipitation, a similar procedure was followed with some modifications[95]. The leaves were grounded in microsome isolation buffer at 4 °C. The cell lysate was filtered through two layers of miracloth, and subjected to centrifugation at 8000 g for 5 min twice to remove debris. The resulting soluble fraction was then performed ultracentrifugation for 30 min at 100,000 g at 4 °C. Both the supernatant and pellet (microsomes) were collected for further experiments.

Construction of sRNA library and data analysis

Total RNA (30 μg) was resolved on 15% urea-PAGE gel, and the 15-30 nt regions were cut from the gel. The sRNAs were recovered by soaking the smashed gel in 0.3 M NaCl overnight, followed by precipitation with ethanol[96]. Then the total sRNAs and sRNAs extracted from AtAGO2 immunoprecipitation were used for sRNA libraries construction using the NEBNext® Small RNA library Prep Set for Illumina® (NEB, E7300S). Two biological replicates of sRNA libraries were constructed and sequenced using an Illumina Hiseq2500 SE50 V4 at Bionova Beijing.

The reads from the Illumina sRNA-seq were processed to remove the 3′ adaptor sequences and low-quality bases using fastp. Clean reads that aligned to rRNA, tRNA, and snoRNA were removed using Bowtie v1.3.0[97], and counts of reads mapped to 45S rRNA region were recorded as normalized background. sRNAs range in length from 18 to 30 nt with perfect matches to the *Arabidopsis* genome sequences (TAIR10 version) were used for further analysis and normalization. To compare sRNAs abundance in *rh3-4* and Col-0 plants, the total sRNA library samples were normalized by calculating their expression levels (reads per million, RPM). sRNAs from the AtAGO2 IP sRNA library were normalized using the number of total 45S rRNA reads[25].

miRNA annotation file was downloaded from miRBase v21, and BEDtools[98] were used to quantify miRNAs, miRNA*s, phasiRNAs, and ta-siRNAs abundance. Adaptor-free reads within 21 and 22 nt were aligned for these regions, allowing for 1-nt shift on either the 5′ or 3′ end. The *TAS* gene regions (*TAS1a*, *1b*, *1c*, *TAS2*, *TAS3a*, *3b*, *3c*, and *TAS4*) were counted and summed separately for each size class (21 nt, 22 nt). A fold change of normalized counts between *rh3-4* and Col-0 greater than 1 and a mean number of reads greater than 10 were considered as significant.

RT-qPCR analysis

Total RNA was extracted from leaves of 4-week-old plants using the RNAprep Pure Plant Kit (Tiangen) according to the manufacturer's instructions. Purified total RNA (1 μg) was used for reverse transcription using the PrimeScript™ RT reagent Kit with gDNA Eraser (Takara). Real-time PCR were performed using TB Green™ *Premix Ex Taq*™ kit (Takara). Primers are listed in Supplementary Data 3. *ACTIN2* was used as the internal control for normalization.

Northern blot

For low molecular weight RNAs, total RNAs or sRNAs extracted from AtAGO2 co-immunoprecipitation beads were separated on 14% urea-polyacrylamide denaturing gels. The gel was transformed to a Hybond membrane NX (GE healthcare) at 14 V overnight. The membrane was chemically crosslinked at 60 °C for 2 h and then incubated at 85 °C for 2 h[99]. The membrane was pre-incubated with PerfectHyb™ Plus Hybridization Buffer liquid (Sigma-Aldrich) for 30 min, then hybridized overnight at 37 °C with ^{32}P-labeled DNA probes. For the detection of endogenous sRNAs, DNA probes reverse complementary to the sRNAs sequences were labeled with γ-^{32}P ATP by T4-polynucleotide kinase. For detection of vsiRNAs, PCR fragment of the CP in TYMV were used to synthesize the α-^{32}P-labeled probes randomly labeled by Prime-a-Gene® Labeling System (Promega) kit[100,101].

For high molecular weight RNAs, freshly infected systemic leaves infected with TYMV (0.1 g) were grounded in liquid nitrogen and RNAs were extracted with hot phenol, and precipitated with 4 M LiCl. 10 μg TYMV RNA was loaded onto a formaldehyde gel and transferred to Hybond membrane N^{+} (GE healthcare) overnight using 20 × SSC (3 M NaCl, 300 mM Sodium Citrate) transfer buffer. Methylene blue staining strip was used as a loading control. The membrane was then UV crosslinked at 1.2×10^5 μJ/cm^2 for 2 min. After pre-incubation with PerfectHyb™ Plus Hybridization Buffer liquid (Sigma-Aldrich) for 30 min, the membrane was then hybridized overnight at 60 °C with α-^{32}P-labeled DNA probes. For virus gRNA detection, PCR fragment of the CP in TYMV were used to synthesize the α-^{32}P-labeled probes randomly labeled by Prime-a-Gene® Labeling System (Promega) kit[100,101]. After hybridization, the membrane was washed with a buffer contains 2 × SSC and 0.025% SDS. Auto-radiography of the membrane was performed using a Typhoon Scanner. Images were quantified with ImageJ. Locked Nucleic Acid probes was used to enhance the sensitivity of Northern blot[102]. Sequences of probes and primers are listed in Supplementary Data 3.

Fluorescence in situ hybridization. In situ hybridization experiments were performed as previously described[103]. Digoxin-labeled RNA probes reverse complementary to miR393b*, miR171 or U6, and biotin-labeled RNA probes reverse complementary to random fragment of chloroplast 16S rRNA were synthesized by BGI. Hypocotyl of 7-day-old Col-0 seedlings were collected and fixed by fixation buffer (120 mM NaCl, 2.7 mM KCl, 0.1% Tween-20, 80 mM EGTA, 5% formaldehyde, and 10% DMSO) under vacuum for 30 min at room temperature. The samples were then dehydrated in a series of solution: 100% methanol for 30 min, 100% ethanol for 30 min, 50% xylene in ethanol for 30 min, 100% ethanol for 30 min, and 100% methanol for 30 min. The samples were further digested with 125 μg/ml proteinase K for 30 min, and incubated with 0.16 M EDC at 60 °C for 2 h. Before hybridization, the samples were rinsed with fixation buffer without formaldehyde and pre-incubated with PerfectHyb™ Plus hybridization buffer for 1 h. Hybridization buffer containing 10 μl of 1 μM DIG-labeled miR393b*, miR171, or U6 probes and 5 μl of 1 μM biotin-labeled 16S rRNA probes were added to the samples. Hybridization was performed overnight at 50 °C. Immunodetection was carried out using Alexa FluorTM 594-conjugated streptavidin (1:200, Invitrogen) and FITC anti-digoxigenin antibody (1:200, Abcam) overnight at 4 °C. Finally, the samples were mounted in Vectashield mounting medium with DAPI and analyzed using a Zeiss LSM710 confocal laser-scanning microscope.

Immunofluorescence analysis of viral dsRNA

To detect TYMV dsRNA, *A. thaliana* seedling infected with TYMV were collected at 5 dpi for protoplast isolation. Immunofluorescence was performed as described previously[104]. Briefly, protoplasts were incubated with 1 volume of fixing solution (4% paraformaldehyde, 0.25 M mannitol, and 50 mM PBS) for 15 min at room temperature. The fixed protoplasts were then washed three times with PBS (10 min each). The fixed protoplasts were transferred onto a cover slide and incubated with 5% BSA in PBS for 20 min at room temperature. The samples were further incubated with monoclonal antibody J2 (1:200, Scicons, 10010500) as the primary antibody and then treated with Alexa Fluor 594-conjugated secondary antibody (1:500, Invitrogen, A-11005). The samples were washed three times with PBS (10 min each) before processing to detect the fluorescence.

Immunoprecipitation and mass spectrometry

Four-week-old *pAGO2::HA-AGO2 in ago2-1* and *p35S::3HA-GFP in* Col-0 plants were harvested and ground in liquid nitrogen. *p35S::3HA-GFP in* Col-0 was served as control. Total proteins were extracted from 3 g ground powder and suspended in 15 ml immunoprecipitation buffer [20 mM Tris-HCl (pH 7.5), 300 mM NaCl, 5 mM MgCl$_2$, 5 mM DTT, 0.5% Tween-20, 1 tablet of cOmplete protease inhibitor per 50 ml] for 10 min at 4 °C. After centrifugation and filtration, the supernatant was immunoprecipitated with 20 μl anti-HA magnetic beads (Lablead) at 4 °C for 2 h. Followed by 4 times washing with washing buffer [250 mM NaCl, 5 mM MgCl$_2$, 5 mM DTT, 20 mM Tris-HCl (pH 7.5), 0.5% Triton X-100, 1 pellet of cOmplete protease inhibitor per 50 ml], proteins copurified with HA-AGO2 or HA-GFP were collected by boiling the beads at 95 °C for 10 min with SDS loading buffer. The pulldown proteins were resolved with 10% SDS-PAGE and the gel band pieces of three biological replicates were cut out and send to Analytical Instrumentation Center of Peking University for Mass spectrometry assay.

The mass spectrometry was done as described previously[105]. Protein samples were digested using the endoproteinase trypsin enzyme. The digested peptides were extracted twice with 5% formic acid/50% acetonitrile. The extracted peptides were vacuum-centrifuged to dryness and resuspended in 0.1% Formic acid in water prior to LC-MS/MS analysis. For LC-MS/MS analysis, the samples were reconstituted in 0.2% formic acid, loaded onto a 100 μm × 2 cm pre-column and separated on a 75 μm × 15 cm capillary column with laser-pulled sprayer. The peptides were separated by the following HPLC gradient: 5-35% B in 60 min, 35-75% B in 4 min, then held at 75% B for 10 min (A = 0.1% formic acid in water, B = 0.1% formic acid in acetonitrile) at a flow rate of 300 nL/min. The eluted peptides were sprayed into a Velos Pro Orbitrap Elite mass spectrometer (Thermo Scientific, USA) equipped with a nano-ESI source. The mass spectrometer was operated in data-dependent mode with a full MS scan (375–1600 M/z) in FT mode at a resolution of 120000 followed by CID (Collision Induced Dissociation) MS/MS scans on the 10 most abundant ions in the initial MS scan.

The acquired mass spectrometry data was further processed using Thermo Proteome Discoverer 2.4 to align with a database downloaded from TAIR (https://www.arabidopsis.org/, version 2021-07-11). Protein differential analysis was processed with DEP pipeline[106]. Briefly, protein abundance matrices from AGO2-IP and GFP-IP were combined and proteins that are only present in one repetition were removed. Variance-stabilized normalization (VSN) was performed as suggested by the DEP pipeline. Left-censored imputation method was used to impute missing values for protein with '0' LFQ intensity. In details, gaussian distribution centered around a minimal value method integrated with DEP was used. Differentially proteins between AGO2-IP and GFP-IP were identified by protein-wise linear models and empirical Bayes statistics. Volcano plot were drawn by R package ggplot2. Proteins in AGO2-IP with p-value < 0.05 and fold change >2 were considered as AGO2 associated proteins, and highlighted in pink box (Supplementary Fig. 2a). The proteins that potentially interacts with AGO2 were listed in Supplementary Fig. 2b with proteins predicted to locate in chloroplast labeled in red.

Phylogenetic analysis

For the phylogenetic analysis of RH3 protein, the RH3 ortholog proteins in 24 plant species (identified or predicted) were used. These

sequences were aligned using ClustalW as implemented within MEGA X. The maximum likelihood bootstrap consensus tree was generated using the JTT matrix-based model with discrete gamma distribution by MEGA X from 500 bootstraps[107,108].

Immunoprecipitation and Co-immunoprecipitation

Immunoprecipitation was performed as previously described[12]. For immunoprecipitation with *Arabidopsis*, 3 g of leaf tissue collected from 4-week-old plants were grounded with liquid nitrogen and resuspended in 15 ml extraction buffer [20 mM Tris-HCl (pH 7.5), 300 mM NaCl, 5 mM $MgCl_2$, 5 mM DTT, 0.5% Tween-20, 1 tablet of cOmplete protease inhibitor per 50 ml]. The protein extracts were then cleared by pre-incubating with 20 µl protein A beads (Invitrogen) for 1 h, and then incubated with 7 µl/g anti-AGO2 antibody (Agrisera, AS132682) overnight at 4 °C. After that, the samples were incubated with 50 µl protein A beads for 1 h and washed three times with washing buffer [20 mM Tris-HCl (pH 7.5), 300 mM NaCl, 5 mM $MgCl_2$, 5 mM DTT, 0.5% Triton X-100, 1 tablet of cOmplete protease inhibitor per 50 ml]. The washed beads were resuspended for further analysis.

For AGO2 immunoprecipitation in supernatant and microsome fractions, purified microsomes were resuspended in 2 ml buffer (a mixture of extraction buffer and microsome isolation buffer in a 1:1 ratio), and 1 ml of supernatant was diluted in a 1:1 ratio with extraction buffer. The ratio of dilution was tested ahead to make sure the level of AGO2 protein in protein extracts is comparable in supernatant and microsome. For AGO2 immunoprecipitation in isolated microsome of Col-0 and *rh3-4*, purified microsomes were resuspended in 2 ml buffer (extraction buffer and microsome isolation buffer mixed with a ratio of 1:1). The protein extracts were cleared by pre-incubating with 5 µl protein A beads (Invitrogen) for 1 h and then incubated with 2 µl/g anti-AGO2 antibody (Agrisera, AS132682) overnight at 4 °C. After that, the products were incubated with 15 µl protein A beads for 1 h, followed with three washes. The washed beads were resuspended for further analysis.

Protein expression and purification. To overcome the difficulty of transient expressing AGO2 in the *E. coli* system, codon optimization was performed on the AGO2 nucleotide sequence. The optimized codon was shown in Supplementary Fig. 4. For the purification of His-tagged recombinant proteins in *E. coli*, the plasmids encoding 6 × His-FLAG-AGO2, 6 × His-TrxA-GST-HA were transformed into BL21 competent cells (DE3), while the plasmids encoding 6 × His-TrxA-RH3-HA and its variants were transformed into Rosetta competent cells (DE3). The transformed cells were grown in LB at 37 °C until reaching an optical density at $OD_{600} = 0.6$. Protein expression was then induced by adding induced with 0.2 mM isopropyl-β-d-thiogalactopyranoside (IPTG) at 16 °C overnight. Subsequent protein purifications were carried out at 4 °C.

The bacterial cells were collected by centrifugation and resuspended in lysis buffer (50 mM phosphate buffer, pH 8.0, 300 mM NaCl, 1% Triton X-100, and 1 tablet of cOmplete EDTA-free protease inhibitor per 50 ml). The cells were then sonicated. After centrifugation, the cleared lysates were loaded onto a HisTrap column with Ni-nitrilotriacetic acid (NTA) resin and washed with 5 ml washing buffer (50 mM phosphate buffer, pH 8.0, 300 mM NaCl, 5 mM imidazole) for three times. The purified proteins were eluted with elution buffer (50 mM phosphate buffer, pH 8.0, 300 mM NaCl, and 300 mM imidazole). The purified AGO2, RH3 and its variants proteins were supplemented with 50% glycerol. The proteins were then frozen using liquid nitrogen and stored at -80 °C.

FLAG pull-down assay

10 µg purified 6 × His-FLAG-AGO2 protein in binding buffer (100 mM NaCl, 20 mM Tris-HCl, pH 7.5, and 0.05% NP-40) was incubated with anti-FLAG M2 agarose beads (Sigma-Aldrich) for 1 h at 4 °C. The beads

were washed three times with binding buffer. After that, the washed beads were incubated with 30 µg 6 × His-GST-HA or 6 × His-RH3-HA, or its variants proteins, respectively. The mixture was rotated at 4 °C for 4 h. After the incubation, beads were washed six times with binding buffer. The beads were boiled at 95 °C for 10 min with SDS loading buffer [25 mM Tris-HCl (pH 6.8), 1% SDS (W/W), 1 mM DTT, 10% glycerol (V/V), 0.01% bromophenol blue]. The eluted proteins were separated on a 10% SDS-PAGE gel and stained with Coomassie brilliant blue R-250.

In vitro RISC assembly assay

An in vitro translation was performed using BYL as described previously with minor modifications[51,109]. Briefly, RH3, mRH3, and GST mRNA was transcribed using SP6 High Yield Message Maker Kit and tailed by A-Plus™ Poly(A) Polymerase Tailing Kit. Subsequently, 1 µg of RH3-HA, mRH3-HA, and GST-HA mRNA were individually translated in a 10 µl BYL translation mixture at 25 °C for 1 h, respectively. Additionally, 1 µg of linearized AGO2 DNA was transcribed and translated using T_NT® Coupled Wheat Germ Extract System (Promega) according to the manufacturer's protocol. After the translation of RH3, mRH3, and GST mRNA in BYL, the AGO2 translation mixture was mixed with the respective RH3, mRH3 or GST samples. sRNA duplexes (100 nM) with 5'-γ-^{32}P labeled passenger strands were added to the translation mixture and incubated at 25 °C for 1 h. 2 µl aliquots of the reaction mixture were transferred into new tubes, and used for Western blots analysis. Anti-FLAG antibody (1:2000, Easybio, BE7003) and anti-HA antibody (1:2000, Easybio, E2061) were used to detect the expression of AGO2 and RH3/mRH3/GST, respectively. 4 µl 5 × Stopping dye solution [500 mM Tris, 450 mM boric acid, 50 mM EDTA, 1 mg/ml bromophenol blue, 1 mg/ml xylene cyanol, 50% (v/v) glycerol] was added to the translation mix and run on native 6% PAGE gel. Radio labeled bands were detected using an image analyzer (Typhoon FLA7000).

Immunofluorescence analysis of protein localization

Immunofluorescence was performed as previously described[85]. *pRH3::RH3-FLAG in rh3-4*, *pAGO2::HA-AGO2 in ago2-1* and *p35S::GFP-HDEL* transgenic plants were used for this assay. 1-week-old seedlings grown on solid 1/2 MS medium were fixed using 4 % paraformaldehyde (Sigma) under vacuum for 60 min at room temperature. For TYMV infected samples, 3-week-old seedlings were used for TYMV inoculation, and systemic leaves were harvested at 7 dpi for fixation. For HA or AGO2 immunofluorescence, cell spreads were incubated with anti-HA (1:200, Abcam, ab18181) or anti-AGO2 (1:200, Agrisera, AS132682) antibody overnight. Goat anti-mouse antibody labeled with Dylight 488 (1:500, Abbkine, A23210) and Dylight 594 labeled goat anti-rabbit antibody (1:1000, Abbkine, A23420) was used as secondary antibody for HA and AGO2, respectively. For dual immunolocalization, cell spreads were first incubated with primary anti-FLAG antibody (1:500, Sigma-Aldrich, F1804) in blocking buffer (2% BSA in 1 × PBS, pH 7.4) at 4 °C overnight Subsequently, the spreads were incubated with either anti-Toc34 (1:200, PhytoAB, PHY1264S) or anti-AGO2 (1:200, Agrisera, AS132682) antibody for 7-8 h at 4 °C. Finally, the spreads were incubated with Dylight 488 labeled goat anti-mouse antibody (1:500, secondary antibody for FLAG) and Dylight 594 labeled goat anti-rabbit antibody (1:1000, secondary antibody for Toc34 and AGO2). Col-0 or *ago2-1* fluorescence was used as a negative control. Images were captured using a Zeiss LSM 710 confocal microscope.

Antibodies

Proteins examined by Western blot were probed by α-AGO2 (1:1000, Agrisera, AS132682), a-Tubulin (1:5000, Easybio, BE0031), α-FLAG (1:2000, Easybio, BE7003), α-HA (1:2000, Easybio, BE2061), α-AGO1 (1:2000, Agrisera, AS09527), α-AGO4 (1:2000, Agrisera, AS09617), α-GFP (1:2000, Easybio, BE2001), α-Toc34 (1:2000, PhytoAB, HY1264S), α-H3 (1:2000, Easybio, BE7004), α-PEPC (1:2000, Agrisera, AS09458),

α-Calnexin (1:2000, Agrisera, AS122365), α-Rbcl (1:2000, Agrisera, AS03037). Secondary antibodies were goat anti-rabbit IgG (1:5000, Easybio, BE0101) and goat anti-mouse IgG (1:5000, Easybio, BE0102). α-PR1 (1:4,000)[12], α-MEMB12 (1:2000)[12], α-CSD2 (1:4,000)[26] have been previously described, and their specificities were validated in paper listed above. Mouse monoclonal α-RH3 (1:2000) was produced by BGI, China, and its specificity was validated in Supplementary Fig. 9c.

Confocal fluorescence microscopy
Agro-infiltrated *N. benthamiana* leaf tissues, transfected protoplast, viral dsRNA, and immunolabelled samples were observed with a Zeiss LSM-710 confocal microscope equipped with Zeiss Zen 2012 software. The following excitation/emission wavelengths were used for specific fluorophores: 405 nm/454-490 nm for CFP, 488 nm/500-540 nm for GFP, 488 nm/510-530 nm for YFP, 561 nm/580-630 nm for RFP/mCherry, and 633 nm/665-721 nm for chlorophyll auto-fluorescence. For the colocalization of RH3-FLAG and AGO2 in immunofluorescence assay, Z stack sequential scanning was performed. Images were digitally captured with a Zeiss Axiocam camera at a 1024- by 1024-pixel resolution and processed with Zen 2.5 2018.

Immunoelectron microscopy
Immunoelectron microscopy was performed as described previously with minor modifications[110]. Briefly, 3-week-old *p35S::RH3-CFP-HA in rh3-4* transgenic plants were cut into pieces and fixed in a fixation buffer (0.1% glutaraldehyde, 3% paraformaldehyde, 0.1 M phosphate, pH 7.2) for 3 h at 4 °C. Samples were then dehydrated in a gradient ethanol series (50%, 70%, 90%, and 100%). The tissue samples were then embedded in K4M resin and polymerized by UV light.

For the immuno-labeling of RH3-HA, a monoclonal α-HA antibody (1:100, Abcam, ab18181) was used as the primary antibody. A gold-coupled anti-mouse antibody (1:200, Sigma-Aldrich, G7652) was used as secondary antibody. The sections were post-stained with aqueous uranyl acetate/lead citrate and examined using a Hitachi H-7650 transmission electron microscope with a CCD camera operating at 80 kV (Hitachi High- Technologies Corporation).

Image intensity analysis
ImageJ version 1.8.0 was used to quantify the Northern blot and the western blot images (https://imagej.nih.gov/ij/index.html). Briefly, the background of images was subtracted with default threshold and integrated densities of the bands were determined. Zeiss Zen (blue edition) with auto threshold was used for the quantification of fluorescence intensity.

Statistics and reproducibility
Statistical parameters were shown in the figure legends. Two-tailed Student's *t* tests were used to determine the difference between two groups. *P*-values were calculated and the cut off for significance was 0.05. P values were presented on the figure. ns: $P > 0.05$, *$P < 0.05$, **$P < 0.01$, ***$P < 0.001$, ***$P < 0.001$, ****$P < 0.0001$. No statistical method was used to predetermine sample size. No data were excluded from the analyses.

Reporting summary
Further information on research design is available in the Nature Portfolio Reporting Summary linked to this article.

Data availability
The mass spectrometry proteomics data have been deposited to the ProteomeXchange Consortium (http://proteomecentral.proteomexchange.org) via the iProX partner repository with the dataset identifier PXD051119[111,112]. The date set of sRNA deep sequencing have been deposited into NCBI under accession numbers PRJNA1096839. The analysis on the AGO2 IP-MS assay and sRNA deep sequencing are available in Supplementary Data 1 and 2. Oligos used in the study are reported in Supplementary Data 3. Source data are provided with this paper.

References
1. Chapman, E. J. & Carrington, J. C. Specialization and evolution of endogenous small RNA pathways. *Nat. Rev. Genet.* **8**, 884–896 (2007).
2. Borges, F. & Martienssen, R. A. The expanding world of small RNAs in plants. *Nat. Rev. Mol. Cell boil.* **16**, 727 (2015).
3. Lopez-Gomollon, S. & Baulcombe, D. C. Roles of RNA silencing in viral and non-viral plant immunity and in the crosstalk between disease resistance systems. *Nat. Rev. Mol. Cell Biol.* **23**, 645–662 (2022).
4. Song, X. et al. MicroRNAs and their regulatory roles in plant-environment interactions. *Annu. Rev. Plant Biol.* **70**, 489–525 (2019).
5. Yu, Y. et al. The 'how' and 'where' of plant microRNAs. *New Phytol* **216**, 1002–1017 (2017).
6. Ding, S. W. RNA-based antiviral immunity. *Nat. Rev. Immunol.* **10**, 632–644 (2010).
7. Huang, J. et al. Diverse functions of small RNAs in different plant–pathogen communications. *Front. Microbiol.* **7**, 1552 (2016).
8. Bologna, N. G. et al. Nucleo-cytosolic shuttling of ARGONAUTE1 prompts a revised model of the plant microRNA pathway. *Mol. Cell* **69**, 709–719 (2018).
9. Ye, R. et al. Cytoplasmic assembly and selective nuclear import of *Arabidopsis* Argonaute4/siRNA complexes. *Mol. Cell* **46**, 859–870 (2012).
10. Zilberman, D. et al. Role of *Arabidopsis* ARGONAUTE4 in RNA-directed DNA methylation triggered by inverted repeats. *Curr. Biol.* **14**, 1214–1220 (2004).
11. Wei, W. et al. A role for small RNAs in DNA double-strand break repair. *Cell* **149**, 101–112 (2012).
12. Zhang, X. et al. *Arabidopsis* argonaute 2 regulates innate immunity via miRNA393*-mediated silencing of a Golgi-localized SNARE gene, *MEMB12*. *Mol. Cell* **42**, 356–366 (2011).
13. Wang, X. et al. The 21-nucleotide, but not 22-nucleotide, viral secondary small interfering RNAs direct potent antiviral defense by two cooperative argonautes in *Arabidopsis thaliana*. *Plant Cell* **23**, 1625–1638 (2011).
14. Harvey, J. J. W. et al. An antiviral defense role of AGO2 in plants. *PLoS One* **6**, e14639 (2011).
15. Garcia-Ruiz, H. et al. Roles and programming of *Arabidopsis* ARGONAUTE proteins during *turnip mosaic virus* infection. *PLoS Pathog* **11**, e1004755 (2015).
16. Jaubert, M. et al. ARGONAUTE2 mediates RNA-silencing antiviral defenses against *potato virus X* in *Arabidopsis*. *Plant Physiol* **156**, 1556–1564 (2011).
17. Scholthof, H. B. et al. Identification of an ARGONAUTE for antiviral RNA silencing in *Nicotiana benthamiana*. *Plant Physiol* **156**, 1548–1555 (2011).
18. Brosseau, C. & Moffett, P. Functional and genetic analysis identify a role for *Arabidopsis* ARGONAUTE5 in antiviral RNA silencing. *Plant Cell* **27**, 1742–1754 (2015).
19. Silva-Martins, G. et al. What does it take to be antiviral? An Argonaute-centered perspective on plant antiviral defense. *J. Exp. Bot.* **71**, 6197–6210 (2020).
20. Wu, H. Here, there, and everywhere: the importance of ER membrane contact sites. *Science* **361**, eaan5835 (2018).
21. Prinz, W. A. et al. The functional universe of membrane contact sites. *Nat. Rev. Mol. Cell Biol.* **21**, 7–24 (2020).
22. Scorrano, L. et al. Coming together to define membrane contact sites. *Nat. Commun.* **10**, 1287 (2019).

23. Schwarz, D. S. & Blower, M. D. The endoplasmic reticulum: structure, function and response to cellular signaling. *Cell. Mol. Life Sci.* **73**, 79–94 (2016).

24. Phillips, M. J. & Voeltz, G. K. Structure and function of ER membrane contact sites with other organelles. *Nat. Rev. Mol. Cell Biol.* **17**, 69–82 (2016).

25. Li, S. et al. Biogenesis of phased siRNAs on membrane-bound polysomes in *Arabidopsis*. *eLife* **5**, e22750 (2016).

26. Li, S. et al. MicroRNAs inhibit the translation of target mRNAs on the endoplasmic reticulum in *Arabidopsis*. *Cell* **153**, 562–574 (2013).

27. Yang, X. et al. Widespread occurrence of microRNA-mediated target cleavage on membrane-bound polysomes. *Genome Biol* **22**, 15 (2021).

28. Margulis, L. *Origin of eukaryotic cells: Evidence and research implications for a theory of the origin and evolution of microbial, plant and animal cells on the precambrian Earth*. Yale University Press (1970).

29. Zhang, J. et al. Full crop protection from an insect pest by expression of long double-stranded RNAs in plastids. *Science* **347**, 991–994 (2015).

30. Gray, M. W. The evolutionary origins of organelles. *Trends Genet* **5**, 294–299 (1989).

31. Helle, S. C. et al. Organization and function of membrane contact sites. *Biochim. Biophys. Acta.* **1833**, 2526–2541 (2013).

32. McLean, B. et al. Continuity of chloroplast and endoplasmic-reticulum membranes in chara and equisetum. *New Phytol* **109**, 59–65 (1988).

33. Andersson, M. X. et al. Membrane contact sites: physical attachment between chloroplasts and endoplasmic reticulum revealed by optical manipulation. *Plant Signal. Behav.* **2**, 185–187 (2007).

34. Andersson, M. X. et al. Optical manipulation reveals strong attracting forces at membrane contact sites between endoplasmic reticulum and chloroplasts. *J. Biol. Chem.* **282**, 1170–1174 (2007).

35. Staehelin, L. A. The plant ER: a dynamic organelle composed of a large number of discrete functional domains. *Plant J* **11**, 1151–1165 (1997).

36. Block, M. A. & Jouhet, J. Lipid trafficking at endoplasmic reticulum–chloroplast membrane contact sites. *Curr. Opin. Cell Biol.* **35**, 21–29 (2015).

37. Hurlock, A. K. et al. Benning C. Lipid trafficking in plant cells. *Traffic* **15**, 915–932 (2014).

38. Rocak, S. & Linder, P. DEAD-box proteins: the driving forces behind RNA metabolism. *Nature Reviews Molecular Cell Biology* **5**, 232–241 (2004).

39. Linder, P. & Jankowsky, E. From unwinding to clamping—the DEAD box RNA helicase family. *Nat. Rev. Mol. Cell Biol.* **12**, 505–516 (2011).

40. Zhang, L. et al. Nucleus-encoded protein BFA1 promotes efficient assembly of the chloroplast ATP synthase coupling factor 1. *Plant Cell* **30**, 1770–1788 (2018).

41. Jelic, M. et al. The chloroplast import receptor Toc34 functions as preprotein-regulated GTPase. *Biol. Chem.* **383**, 1875–1883 (2002).

42. Nelson, B. K. et al. A multicolored set of in vivo organelle markers for co-localization studies in *Arabidopsis* and other plants. *Plant J* **51**, 1126–1136 (2007).

43. Mathur, J. et al. Membrane contacts with the endoplasmic reticulum modulate plastid morphology and behaviour. *Front. Plant Sci.* **14**, 1293906 (2023).

44. Sohrt, K. & Soll, J. Toc64, a new component of the protein translocon of chloroplasts. *J. Cell Biol.* **148**, 1213–1221 (2000).

45. Schaad, M. C. et al. Formation of plant RNA virus replication complexes on membranes: role of an endoplasmic reticulum-targeted viral protein. *EMBO journal* **16**, 4049–4059 (1997).

46. Wei, T. et al. Sequential recruitment of the endoplasmic reticulum and chloroplasts for plant potyvirus replication. *J. Virol.* **84**, 799–809 (2010).

47. Wei, T. et al. The SNARE protein Syp71 is essential for turnip mosaic virus infection by mediating fusion of virus-induced vesicles with chloroplasts. *PLoS Pathogens* **9**, e1003378 (2013).

48. Asakura, Y. et al. Chloroplast RH3 DEAD box RNA helicases in maize and *Arabidopsis* function in splicing of specific group II introns and affect chloroplast ribosome biogenesis. *Plant Physiol* **159**, 961–974 (2012).

49. Gu, L. et al. A chloroplast-localized DEAD-box RNA helicase AtRH3 is essential for intron splicing and plays an important role in the growth and stress response in *Arabidopsis thaliana*. *Plant Physiol. Biochem.* **82**, 309–318 (2014).

50. Fang, X. et al. Chloroplast-to-nucleus signaling regulates microRNA biogenesis in *Arabidopsis*. *Dev. Cell* **48**, 371–382 (2019).

51. Iki, T. et al. In vitro assembly of plant RNA-induced silencing complexes facilitated by molecular chaperone HSP90. *Mol. Cell* **39**, 282–291 (2010).

52. Woo, H. R. et al. Programming of plant leaf senescence with temporal and inter-organellar coordination of transcriptome in *Arabidopsis*. *Plant Physiol* **171**, 452–467 (2016).

53. Dreher, T. W. Turnip yellow mosaic virus: transfer RNA mimicry, chloroplasts and a C-rich genome. *Mol. Plant Pathol.* **5**, 367–375 (2004).

54. Zhao, J. et al. Chloroplast in plant-virus interaction. *Front. Microbiol.* **7**, 1565 (2016).

55. Bhattacharyya, D. & Chakraborty, S. Chloroplast: the trojan horse in plant-virus interaction. *Mol. Plant Pathol.* **19**, 504–518 (2018).

56. Heinlein, M. Plant virus replication and movement. *Virol* **479**, 657–671 (2015).

57. Laliberté, J.-F. & Sanfaçon, H. Cellular remodeling during plant virus infection. *Annu. Rev. Phytopathol.* **48**, 69–91 (2010).

58. Prod'homme, D., Jakubiec, A., Tournier, V., Drugeon, G. & Jupin, I. Targeting of the Turnip Yellow Mosaic Virus 66K replication protein to the chloroplast envelope is mediated by the 140K protein. *J. Virol.* **77**, 9124–9135 (2003).

59. Prod'homme, D., Le Panse, S., Drugeon, G. & Jupin, I. Detection and subcellular localization of the turnip yellow mosaic virus 66K replication protein in infected cells. *Virol* **281**, 88–101 (2001).

60. Moriceau, L., Jomat, L., Bressanelli, S., Alcaide-Loridan, C. & Jupin, I. Identification and Molecular Characterization of the Chloroplast Targeting Domain of Turnip yellow mosaic virus Replication Proteins. Front. Plant Sci. **8**, (2017).

61. Bouche, N. et al. An antagonistic function for *Arabidopsis* DCL2 in development and a new function for DCL4 in generating viral siRNAs. *EMBO J* **25**, 3347–3356 (2006).

62. Wang, X. et al. RNAi-mediated viral immunity requires amplification of virus-derived siRNAs in *Arabidopsis thaliana*. *Proc. Natl. Acad. Sci. Usa.* **107**, 484–489 (2010).

63. Sehki, H., Yu, A., Elmayan, T. & Vaucheret, H. TYMV and TRV infect *Arabidopsis thaliana* by expressing weak suppressors of RNA silencing and inducing host RNASE THREE LIKE1. *Plos Pathogens* **19**, (2023).

64. Fang, X. & Qi, Y. RNAi in plants: an Argonaute-centered view. *Plant Cell* **28**, 272–285 (2016).

65. Qu, F. et al. *Arabidopsis* DRB4, AGO1, AGO7, and RDR6 participate in a DCL4-initiated antiviral RNA silencing pathway negatively regulated by DCL1. *Proc. Natl. Acad. Sci. Usa.* **105**, 14732–14737 (2008).

66. Gregory, B. D. et al. A link between RNA metabolism and silencing affecting *Arabidopsis* development. *Dev. Cell* **14**, 854–866 (2008).

67. Brodersen, P. et al. Isoprenoid biosynthesis is required for miRNA function and affects membrane association of ARGONAUTE 1 in *Arabidopsis*. *Proc. Natl. Acad. Sci. Usa.* **109**, 1778–1783 (2012).

68. Jouannet, V. et al. Cytoplasmic *Arabidopsis* AGO7 accumulates in membrane-associated siRNA bodies and is required for ta-siRNA biogenesis. *EMBO J* **31**, 1704–1713 (2012).

69. Hou, C. Y. et al. Global analysis of truncated RNA ends reveals new insights into ribosome stalling in plants. *Plant Cell* **28**, 2398–2416 (2016).

70. Jiang, J. & Laliberté, J. F. Membrane association for plant virus replication and movement. *Current Research Topics in Plant Virology*. Springer International Publishing (2016).

71. Ravindran, M. S. et al. Tsai B. Opportunistic intruders: how viruses orchestrate ER functions to infect cells. *Nat. Rev. Microbiol.* **14**, 407–420 (2016).

72. Patarroyo, C. et al. Hijack it, change it: how do plant viruses utilize the host secretory pathway for efficient viral replication and spread? *Front. Plant Sci* **3**, 308 (2012).

73. Wang, P. et al. Plant endoplasmic reticulum–plasma membrane contact sites. *Trends Plant Sci* **22**, 289–297 (2017).

74. Pérez-Sancho, J. et al. Stitching organelles: organization and function of specialized membrane contact sites in plants. *Trends Cell Biol* **26**, 705–717 (2016).

75. Levy, A. et al. Synaptotagmin SYTA forms ER-plasma membrane junctions that are recruited to plasmodesmata for plant virus movement. *Curr. Biol.* **25**, 2018–2025 (2015).

76. Barajas, D. et al. Co-opted oxysterol-binding ORP and VAP proteins channel sterols to RNA virus replication sites *via* membrane contact sites. *PLoS Pathog* **10**, e1004388 (2014).

77. Carette, J. E. et al. van Kampen T, Wellink J, van Kammen A. Characterization of plant proteins that interact with *cowpea mosaic virus '60K'* protein in the yeast two-hybrid system. *J. Gen. Virol.* **83**, 885–893 (2002).

78. Brosseau, C. et al. Moffett P. Antiviral defense involves AGO4 in an *Arabidopsis*-Potexvirus Interaction. *Mol. Plant Microbe Interact.* **29**, 878–888 (2016).

79. Dalmadi, Á. et al. AGO-unbound cytosolic pool of mature miRNAs in plant cells reveals a novel regulatory step at AGO1 loading. *Nucleic Acids Res* **47**, 9803–9817 (2019).

80. Fan, L. et al. Microtubules promote the non-cell autonomous action of microRNAs by inhibiting their cytoplasmic loading onto ARGONAUTE1 in *Arabidopsis*. *Dev. Cell* **57**, 995–1008 (2022).

81. Velikanov, G. Endoplasmic reticulum: membrane contact sites. *Cell Tissue Biol* **7**, 504–511 (2013).

82. Saheki, Y. & Camilli, P. D. Endoplasmic reticulum–plasma membrane contact sites. *Annu. Rev. Biochem.* **86**, 659–684 (2017).

83. Rowland, A. A. & Voeltz, G. K. Endoplasmic reticulum-mitochondria contacts: function of the junction. *Nat. Rev. Mol. Cell Biol.* **13**, 607–625 (2012).

84. Clough, S. J. & Bent, A. F. Floral dip: a simplified method for Agrobacterium-mediated transformation of *Arabidopsis thaliana*. *Plant J* **16**, 735–743 (1998).

85. Li, Q. et al. DEAD-box helicases modulate dicing body formation in *Arabidopsis*. *Sci. Adv.* **7**, eabc6266 (2021).

86. Zanetti, M. E. et al. Immunopurification of polyribosomal complexes of *Arabidopsis* for global analysis of gene expression. *Plant Physiol* **138**, 624–635 (2005).

87. Earley, K. W. et al. Gateway-compatible vectors for plant functional genomics and proteomics. *Plant J* **45**, 616–629 (2006).

88. Curtis, M. D. & Grossniklaus, U. A gateway cloning vector set for high-throughput functional analysis of genes in planta. *Plant Physiol* **133**, 462–469 (2003).

89. Martin, K. et al. Transient expression in *Nicotiana benthamiana* fluorescent marker lines provides enhanced definition of protein localization, movement and interactions in planta. *Plant J* **59**, 150–162 (2009).

90. Tong, X. et al. A small peptide inhibits siRNA amplification in plants by mediating autophagic degradation of SGS3/RDR6 bodies. *EMBO J* **40**, e108050 (2021).

91. Wang, D. et al. Induction of protein secretory pathway is required for systemic acquired resistance. *Science* **308**, 1036–1040 (2005).

92. Garcia-Ruiz, H. et al. Arabidopsis RNA-dependent RNA polymerases and dicer-like proteins in antiviral defense and small interfering RNA biogenesis during Turnip Mosaic Virus infection. *Plant Cell* **22**, 481–496 (2010).

93. Marion, J. et al. Systematic analysis of protein subcellular localization and interaction using high-throughput transient transformation of Arabidopsis seedlings. *Plant J* **56**, 169–179 (2008).

94. Yoo, S.-D. et al. *Arabidopsis* mesophyll protoplasts: a versatile cell system for transient gene expression analysis. *Nat. Protoc.* **2**, 1565–1572 (2007).

95. LaMontagne, E. D. et al. Isolation of microsomal membrane proteins from *Arabidopsis thaliana*. *Curr. Protoc. Plant Biol.* **1**, 217–234 (2016).

96. Liu, Y. et al. AtXRN4 affects the turnover of chosen miRNA*s in *Arabidopsis*. *Plants-Basel* **9**, 362 (2020).

97. Langmead, B. et al. Ultrafast and memory-efficient alignment of short DNA sequences to the human genome. *Genome Biol* **10**, R25 (2009).

98. Quinlan, A. R. & Hall, I. M. BEDTools: a flexible suite of utilities for comparing genomic features. *Bioinformatics* **26**, 841–842 (2010).

99. Pall, G. S. et al. Carbodiimide-mediated cross-linking of RNA to nylon membranes improves the detection of siRNA, miRNA and piRNA by northern blot. *Nucleic Acids Res* **35**, e60 (2007).

100. Cao, M. et al. Virus infection triggers widespread silencing of host genes by a distinct class of endogenous siRNAs in *Arabidopsis*. *Proc. Natl. Acad. Sci. USA* **111**, 14613–14618 (2014).

101. Shamandi, N. et al. Plants encode a general siRNA suppressor that is induced and suppressed by viruses. *PLoS Biol* **13**, e1002326 (2015).

102. Várallyay, É., Burgyán, J. & Havelda, Z. MicroRNA detection by northern blotting using locked nucleic acid probes. *Nat. Protoc.* **3**, 190–196 (2008).

103. Zhu, P. et al. *Arabidopsis* small nucleolar RNA monitors the efficient pre-rRNA processing during ribosome biogenesis. *Proc. Natl. Acad. Sci. USA* **113**, 11967–11972 (2016).

104. Cotton, S. et al. *Turnip mosaic virus* RNA replication complex vesicles are mobile, align with microfilaments, and are each derived from a single viral genome. *J. Virol.* **83**, 10460–10471 (2009).

105. Li, Q. et al. Regulation of active DNA demethylation by a methyl-CpG-binding domain protein in *Arabidopsis thaliana*. *PLoS Genet* **11**, e1005210 (2015).

106. Zhang, X. et al. Proteome-wide identification of ubiquitin interactions using UbIA-MS. *Nat Protoc* **13**, 530–550 (2018).

107. Jones, D. T. et al. The rapid generation of mutation data matrices from protein sequences. *Comput. Appl. Biosci.* **8**, 275–282 (1992).

108. Kumar, S. et al. MEGA X: molecular evolutionary genetics analysis across computing platforms. *Mol. Biol. Evol.* **35**, 1547–1549 (2018).

109. Buntru, M. et al. Tobacco BY-2 cell-free lysate: an alternative and highly-productive plant-based in vitro translation system. *BMC Biotechnol* **14**, 37 (2014).

110. Bendayan, M. & Zollinger, M. Ultrastructural localization of antigenic sites on osmium-fixed tissues applying the protein A-gold technique. *J. Histochem. Cytochem.* **31**, 101–109 (1983).

111. Ma, J. et al. iProX: an integrated proteome resource. *Nucleic Acids Res.* **47**, D1211–D1217 (2019).

112. Chen, T. et al. iProX in 2021: connecting proteomics data sharing with big data. *Nucleic Acids Res.* **50**, D1522–D1527 (2022).

Acknowledgements

Author contributions

Conceptualization, X.Z.; Methodology, J.H., and J.D.; Investigation, J.H., J.D., Yan.L., Y.X., Y.C., Q.Liu., M.D., Yang.L., Y.Z., L.H., W.W., C.D.,; Formal Analysis, L.L, J.S.; Writing – Original Draft, X.Z., F.C., J.H., and J.D.; Writing –Review & Editing, X.Z., F.C., J.C., Y-W.Y., R.L., J.W., L.W., and Q.Li.; Funding Acquisition, X.Z., and Q.Li.; Supervision, X.Z., F.C., and L.W.

Competing interests

The authors declare no competing interests.

Additional information

Supplementary information The online version contains supplementary material available at https://doi.org/10.1038/s41467-025-57296-6.

Correspondence and requests for materials should be addressed to Feng Cui or Xiaoming Zhang.

Peer review information *Nature Communications* thanks Gaoyuan Song, and the other, anonymous, reviewer(s) for their contribution to the peer review of this work. A peer review file is available.

Reprints and permissions information is available at http://www.nature.com/reprints

Publisher's note Springer Nature remains neutral with regard to jurisdictional claims in published maps and institutional affiliations.